remote sensing

MDPI

Article

Soil Organic Carbon Estimation from UAV Hyperspectral Data Using TOPSIS-Based Band Selection and Stacking Ensemble Learning

Lingbo Wang, Yufeng Wang *, Kai Liu, Nan Liu, Qing Yan and Dengxin Hua

School of Optoelectronic Science and Intelligent Instrumentation, Xi'an University of Technology, Xi'an 710048, China; 2240220114@stu.xaut.edu.cn (L.W.); 1200211023@stu.xaut.edu.cn (K.L.); 2250221173@stu.xaut.edu.cn (N.L.); yanqing@xaut.edu.cn (Q.Y.); dengxinhua@xaut.edu.cn (D.H.)
* Correspondence: wangyufeng@xaut.edu.cn

Highlights

What are the main findings?

- The RFE–TOPSIS method selected 12 optimal SOC bands from hyperspectral data, effectively reducing spectral redundancy for SOC estimation.
- A stacking ensemble model yielded accurate SOC prediction performance on the validation set (R^2 = 0.85, RMSE = 0.96 g/kg, RPD = 2.47), outperforming individual base models.

What are the implications of the main findings?

- Methodologically, the hybrid feature selection and stacking strategy simultaneously enhances estimation accuracy for SOC prediction in cultivated land.
- Practically, the proposed framework supports UAV-based field-scale SOC estimation, providing valuable information for precision agriculture and soil carbon accounting.

Abstract

Rapid and accurate soil organic carbon (SOC) quantification from UAV hyperspectral data is challenged by spectral redundancy and the limited generalization of individual models. This study proposes an RFE–TOPSIS–stacking method, a hybrid feature selection and stacking ensemble framework for SOC estimation using UAV hyperspectral data (350–1002 nm). Recursive feature elimination (RFE) based on XGBoost was first employed for preliminary band screening, retaining 19 bands. Then, the Technique for Order Preference by Similarity to Ideal Solution (TOPSIS), a multi-criteria decision-making method, was applied to comprehensively evaluate these bands using mutual evaluation, integrating mutual information, entropy, random forest importance, the inverse coefficient of variation of reflectance, and band redundancy, and was then applied to select 12 SOC characteristic bands. A stacking regression model was subsequently constructed using a 1D-CNN, SVR, XGBoost, and PLSR as base learners and random forest as the meta-learner. The framework achieved an R^2 of 0.85, an RMSE of 0.96 g/kg, and an RPD of 2.47 for the validation set, outperforming the individual model (1D-CNN: R^2 = 0.78, RMSE = 1.05 g/kg, and RPD =2.26). Application to the three study areas revealed SOC contents (P10–P90) of 7.37–9.59, 7.52–11.01, and 9.98–15.43 g/kg; most validation sampling points had absolute residuals < 1 g/kg (max: 1.65 g/kg), and approximately 80% had relative errors within ±10%. The proposed framework provides a methodological basis for UAV-based field-scale SOC estimation and spatial mapping, with potential applications in precision agriculture and soil carbon assessment.

Check for updates

Academic Editor: Mohammadmehdi Saberioon

Received: 24 September 2026
Revised: 2 November 2026
Accepted: 4 November 2026
Published: 6 November 2026

Copyright: © 2026 by the authors. Licensee MDPI, Basel, Switzerland. This article is an open access article distributed under the terms and conditions of the Creative Commons Attribution (CC BY) license.

Keywords: soil organic carbon; UAV hyperspectral; characteristic band selection; TOPSIS; machine learning; hyperspectral remote sensing

1. Introduction

Soil organic carbon (SOC) is an important component of soil organic matter and a core indicator of soil fertility [1]. SOC not only directly affects soil structure and nutrient retention capacity but also has an important influence on crop growth and agricultural productivity [2,3]. As an important component of the soil carbon pool, SOC accounts for approximately 50–80% of the total soil carbon storage and plays a key role in the global carbon cycle and climate regulation [4]. Therefore, accurately obtaining SOC contents and their spatial distributions in farmland is essential for the effective utilization of soil resources, sustainable agricultural development, and farmland carbon sequestration management under the "dual carbon" goals.

Traditional methods for measuring SOC content mainly rely on laboratory chemical analysis, such as the dry combustion method and potassium dichromate external heating method (Walkley–Black method); however, meeting the requirements of large-scale batch analysis is difficult because of the complex testing procedure and the amount of time and labor required [5]. Remote sensing images integrating spectral and spatial information provide a reliable technical approach for SOC estimation. Earlier research focused on multispectral satellite remote sensing to estimate SOC [6]. Li et al. estimated the SOC content in the Bosten Lake Basin using Sentinel-2 multispectral satellite data [7]. In comparison, hyperspectral remote sensing can acquire hundreds of continuous, narrow spectral bands, providing richer data support for fine-scale SOC inversion [8–11]. Meng et al. estimated the SOC of farmland in Northeast China using hyperspectral satellite data from the Gaofen-5 satellite, and the coefficient of determination (R^2) of the established SVM model reached 0.80 [12]. However, satellite-based hyperspectral remote sensing still suffers from limitations, such as low spatial resolution and long satellite revisit periods, making it difficult to meet the requirements of highly time-efficient and high-precision SOC monitoring. In recent years, UAV hyperspectral remote sensing has been widely applied to the monitoring of soil nutrients and soil physicochemical properties because of its high spatial and spectral resolution [13–15]. Yang et al. combined UAV hyperspectral data with a one-dimensional convolutional neural network to predict the SOC at a farm in Heilongjiang Province, and the R^2 of the model reached 0.84 [16]. Zhu et al. investigated the possibility of applying laboratory hyperspectral models for loess areas in Belgium and black soil areas in Northeast China; the R^2 and RPD of the validation set reached 0.66 and 1.72, respectively [17].

With continuous development, the extraction of spectral characteristic bands from high-dimensional spectral data has become a key factor affecting model accuracy and stability. To address the high dimensionality and severe information redundancy in UAV hyperspectral data, researchers at home and abroad have explored methods for characteristic band extraction, including the filter method based on random forests and mathematical transformations [18,19], embedded methods, such as partial least squares–variable importance in projection and the iterative retention of informative variables [20,21], and the wrapper method based on particle swarm optimization and grey wolf optimization algorithms [22]. For example, Gu et al. proposed wavelet transformation combined with the random forest algorithm to select characteristic bands from hundreds of spectral bands, thereby improving the SOC prediction accuracy [23]. Zhang et al. successfully extracted 16 characteristic bands of SOC by using mathematical transformations and the iterative retention of informative variables (IRIV) [24]. Han et al. achieved high-precision SOC

prediction in the Songnen Plain using a Transformer model [25]. Although existing studies have made considerable progress in hyperspectral characteristic band extraction, the scientificity, stability, and interpretability of the characteristic band extraction process still need further improvement. Meanwhile, a single model often suffers from insufficient generalization ability under complex soil environments. Thus, developing an accurate and robust framework for SOC monitoring is still challenging but necessary.

In this study, an RFE–TOPSIS–stacking framework is proposed for SOC prediction. Specifically, recursive feature elimination (RFE) is first employed to preliminarily screen the hyperspectral bands, followed by the Technique for Order Preference by Similarity to Ideal Solution (TOPSIS), a multi-criteria decision-making method, to comprehensively evaluate and select informative spectral bands predictive of SOC. Finally, a stacking ensemble regression model is employed for SOC estimation. The experiments and methods are illustrated in Section 2, including the UAV hyperspectral image acquisition and soil sample collection, as well as the principles and implementation of the RFE–TOPSIS method for the characteristic band extraction and the stacking ensemble regression model. The results are presented in Section 3. The 19 characteristic band subsets and the further 12 characteristic bands are provided in detail, and the constructed stacking model and the estimation of SOC are also investigated. The optimal stacking model applied to UAV hyperspectral imagery to generate SOC maps for the three study areas. Section 4 further analyzes and discusses. Section 5 presents the conclusions.

2. Materials and Methods

2.1. UAV Hyperspectral Image Acquisition and Soil Sample Collection

In this study, three typical farmlands in Jingyang County, Xianyang City, Shaanxi Province, China (108°44′E, 34°37′N), were selected as the study areas and are shown in Figure 1. The surface conditions of the three study areas were as follows: Areas A and B covered 2.22 ha and 7.48 ha, respectively, and both were under wheat–maize rotation systems. Area C covered 3.00 ha and was primarily cultivated with crops such as cauliflower, cabbage, and kohlrabi. All three study areas had been plowed before sampling, and their soil surfaces were almost free of wheat stubble and straw residues. The average soil moisture was 2.5%. A DJI M350 UAV (SZ DJI TECHNOLOGY Co., Ltd., Shenzhen, China) equipped with an X20P Vis-Near hyperspectral imaging sensor (Cubert GmbH, Ulm, Germany) was used for data acquisition. The flight was conducted at midday on 17 July 2025, under clear weather conditions and wind speeds below 3 m/s, with a solar elevation angle of approximately 75–79°. The relatively high solar elevation angle helped reduce the influence of illumination-related artifacts on the spectral data. The UAV was operated at a flight altitude of 100 m to acquire hyperspectral images, with a ground sampling distance (GSD) of 3.39 cm, a spectral range of 350–1002 nm, a spectral resolution of 4 nm, and a total of 164 spectral bands. A total of 95,968,140 pixels were collected across the three study areas.

Before spectral data acquisition, radiometric calibration was performed to reduce the interference of environmental conditions and instrument noise. The specific procedures were as follows: (1) placement of the diffuse reflection panel and parameter initialization; (2) reflectance correction using the diffuse reflection panel; (3) dark-current correction; (4) radiometric calibration.

As an example, the hyperspectral images of area B are presented in Figure 2, where Figure 2a–c show the single-band images at 470, 794, and 950 nm, respectively, and Figure 2d corresponds to the RGB color composite image. These images reflect the spectral response characteristics of the soil at different wavelengths. The image at 470 nm is relatively smooth, while the 794 nm near-infrared band delivers sharper field-block textures and surface features. In contrast, the image at 950 nm is strongly affected by water vapor and soil

moisture absorption, which weakens the surface signal and obscures textural details. The RGB color composite image provides a more intuitive representation of the field tillage areas, field boundaries, and other spatial features. Figure 3 shows the soil reflectance spectral curves. These curves were derived from the mean spectra of all pixels within a subarea of 1 m × 1 m. Overall, the reflectance values are mainly distributed within the range of 0.02–0.46, and the spectral curves exhibit generally consistent trends, indicating relatively consistent spectral response characteristics of the soils in the study area. Specifically, in the visible region (350–780 nm), the spectral reflectance continuously increases with the wavelength, and a weak absorption peak appears near 450 nm. In the range of 780–900 nm, the rate of increase in reflectance gradually decreases. Near 950 nm, a distinct valley appears, indicating a strong water absorption region and a relatively high sensitivity to variations in the soil moisture content.

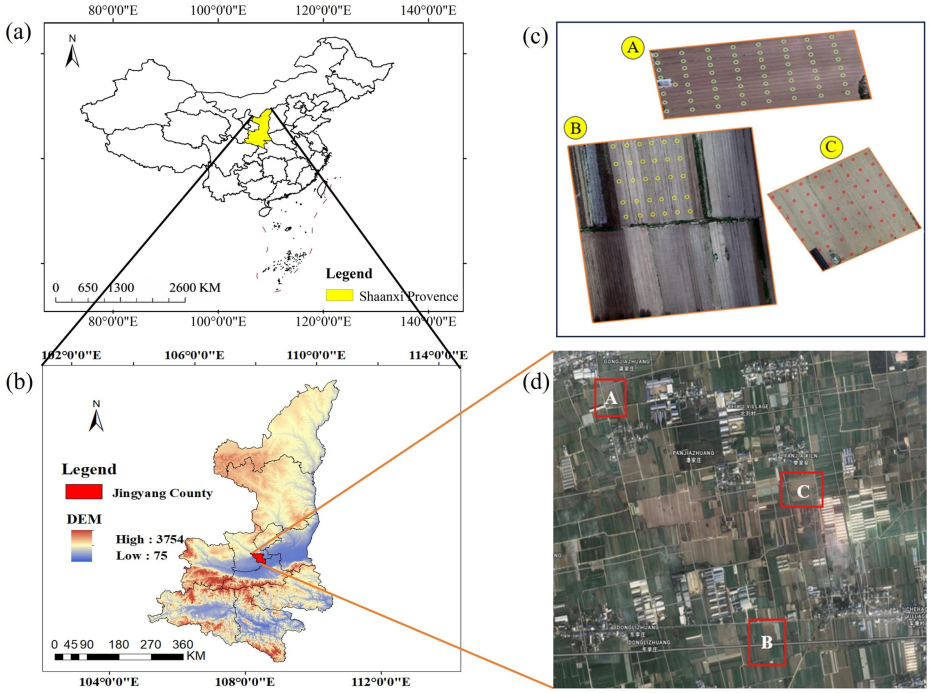


Figure 1. Locations of study areas: (**a**) Location of Shaanxi Province; (**b**) DEM and location of Jingyang County; (**c**) Relative locations of the three study areas; (**d**) UAV imagery and sampling sites.

Soil samples were also collected during the experiment with the UAV hyperspectral data. A total of 144 soil samples were simultaneously collected, including 62 samples in area A, 29 samples in area B, and 53 samples in area C. It should be pointed out that soil samples in area B were collected only from a portion of the area, resulting in a relatively small number of sampling points despite its larger spatial extent. Each sampling subarea was georeferenced using a handheld GPS, and a composite soil sample of approximately 1 kg was collected from the 0–20 cm topsoil layer within each 1 m × 1 m subarea using the five-point sampling method. After removing impurities such as stones and plant and animal residues, the soil samples were thoroughly mixed, placed into sealed bags, and labeled accordingly. After sampling, all soil samples were sent to the Central Laboratory of the China Chemical Geology and Mine Bureau for SOC content determination using the potassium dichromate oxidation method with external heating. Laboratory quality control procedures included blank tests, certified reference material analyses, and parallel sample measurements to ensure the reliability of SOC determination. The measured SOC contents of the soil samples are shown in Figure 4a, and the corresponding statistical results are presented in Figure 4b. Significant differences in SOC contents were observed among

the three study areas. Area C exhibited the highest SOC content, with median and mean values higher than those of areas A and B, as well as a relatively wider distribution range. In contrast, areas A and B had relatively lower SOC contents. The sample set partitioning based on joint X–Y distances (SPXY) method was employed to divide the 144 samples into training and validation sets by jointly considering distances in the spectral feature space (X) and the SOC response space (Y), rather than solely by SOC content; thus, the distribution of samples across SOC ranges was also affected by the joint X–Y distances among samples. The training-to-validation ratio was set to 7:3, resulting in 100 training samples and 44 validation samples. The descriptive statistics are presented in Table 1. The training set consisted of 100 samples, with SOC contents ranging from 6.37 to 16.48 g/kg, a mean of 10.00 g/kg, and a standard deviation of approximately 2.80 g/kg. The validation set contained 44 samples, with SOC contents ranging from 6.00 to 16.58 g/kg, a mean of 8.92 g/kg, and a standard deviation of approximately 2.37 g/kg. Overall, the SOC contents across the study areas ranged from 6.00 to 16.58 g/kg, with a mean of 9.67 g/kg and a standard deviation of 2.72 g/kg. Among them, only the training-set samples were used to extract the SOC characteristic bands and train the model, while the validation-set samples were solely used to verify the model's predictive ability.

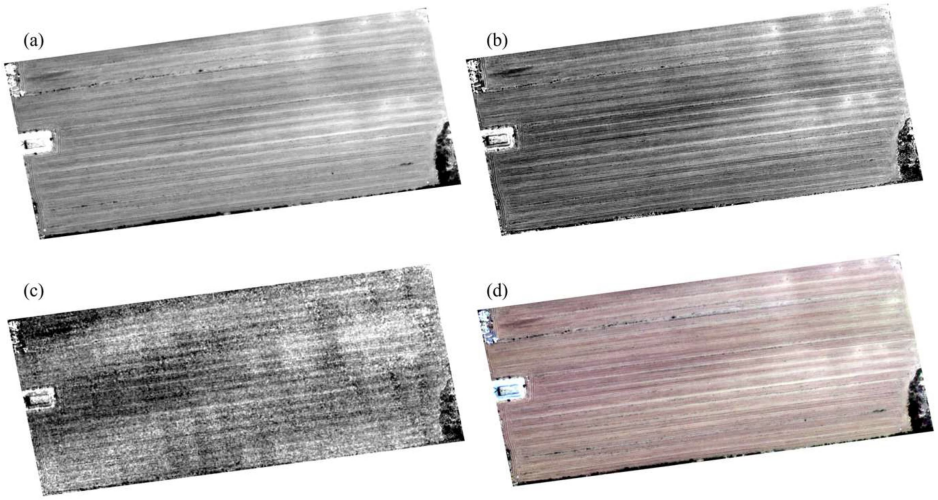


Figure 2. Single-band and RGB images of study area A: (**a**) 470 nm; (**b**) 794 nm; (**c**) 950 nm; (**d**) RGB.

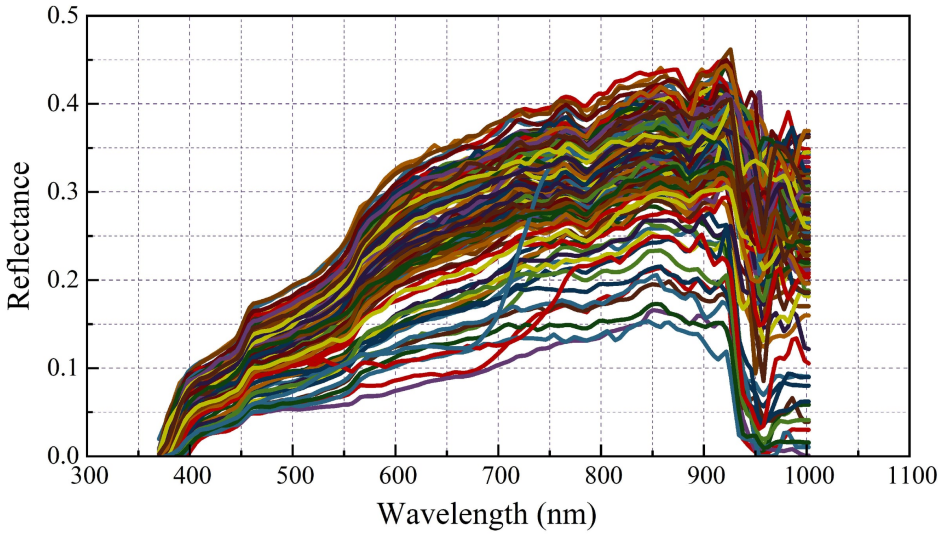


Figure 3. Spectral reflectance curves of soil samples.

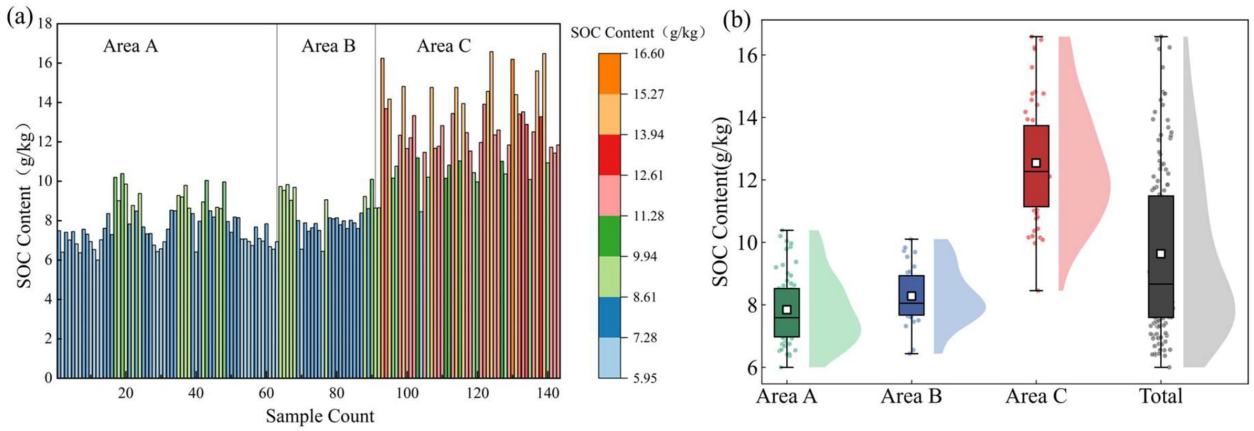


Figure 4. Statistics of SOC contents in study areas: (**a**) SOC contents of sampling locations; (**b**) distribution patterns of SOC contents at sampling locations.

Table 1. Statistical results of SOC contents in 144 soil samples.

Dataset	Total Sample	Training Set	Validation Set
Sample size	144	100	44
Maximum (g/kg)	16.58	16.48	16.58
Minimum (g/kg)	6.00	6.37	6.00
Mean (g/kg)	9.67	10.00	8.92
Median (g/kg)	8.66	9.40	8.14
Skewness	0.98	0.81	1.50
Kurtosis	0.35	0.06	1.98
Standard deviation (g/kg)	2.72	2.80	2.37

2.2. Characteristic Band Extraction Based on RFE–TOPSIS

Hyperspectral remote sensing technology provides high spectral resolution and abundant spectral information; however, hyperspectral data also suffer from high spectral dimensionality and strong correlations among adjacent bands, which not only increase the computational complexity of the model but may also reduce its stability and generalization ability. Therefore, characteristic band extraction is an important prerequisite for high-precision inversion using hyperspectral remote sensing data. In this study, the process of the spectral characteristic band extraction was conducted in two steps: (1) a characteristic band subset was obtained using RFE; (2) the TOPSIS was employed to rank the comprehensive closeness of the characteristic band subset and extract the SOC characteristic bands. The specific procedure is shown in Figure 5.

2.2.1. Preliminary Selection of Characteristic Band Subsets Based on RFE

Recursive feature elimination (RFE) is a classical feature selection method that progressively eliminates features with relatively low contributions through recursive iterations [26]. In this study, extreme gradient boosting (XGBoost), which has strong capability in feature importance evaluation, was combined with the backward iterative search mechanism of RFE to preliminarily reduce the dimensionality of the spectral characteristic bands for SOC.

XGBoost establishes a prediction model by integrating multiple regression trees, and its prediction function can be expressed as follows:

$$\hat{y}_i = \sum_{k=1}^{K} f_k(x_i),\ f_k \in F \quad (1)$$

where x_i represents the input feature, $\hat{y}_i$ represents the predicted SOC content, K represents the number of regression trees, f_k represents the k regression tree, and K denotes the space of regression trees.

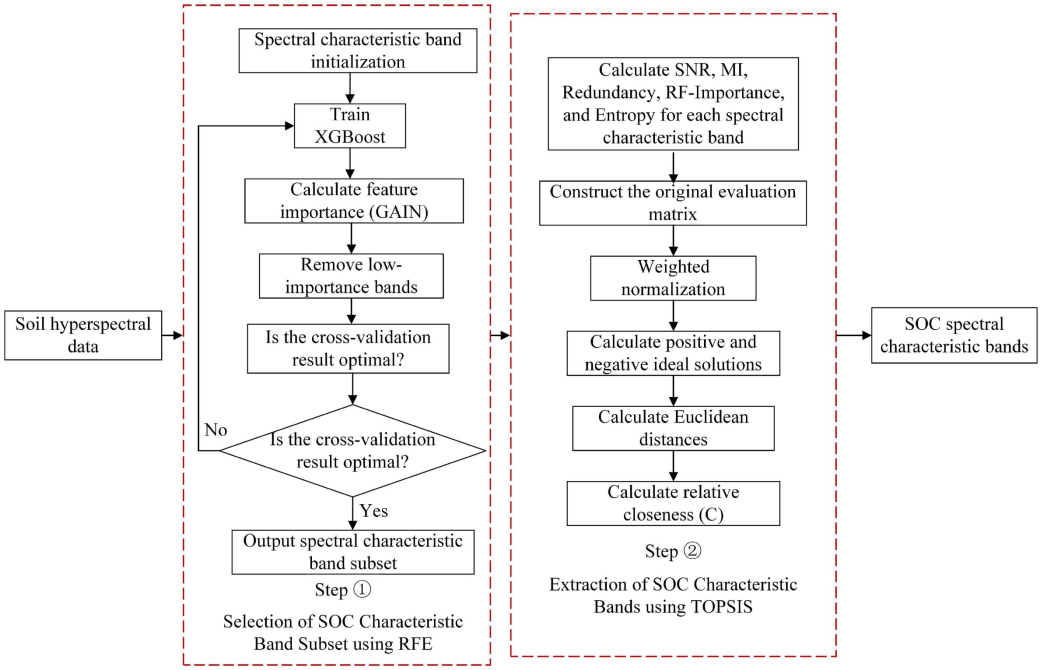


Figure 5. Workflow of spectral characteristic band selection based on RFE–TOPSIS.

XGBoost is based on the second-order Taylor expansion of the objective function and uses the split gain (Gain) to measure the loss reduction resulting from node splitting. After model training, the contribution of each band to the objective function gain can be calculated to obtain the corresponding feature importance, which is subsequently used as the basis for recursive feature selection in the RFE. After obtaining the importance of each band, a backward recursive search strategy for characteristic band extraction is adopted in the RFE. Let the initial feature set be $S^{(0)} = \{x_1, x_2, \cdots x_{164}\}$. At the k iteration, the XGBoost model is retrained to calculate the importance (I_j) of each band in the current feature set. Subsequently, the band with the lowest feature importance can be removed:

$$x_r = \arg\min_{x_j \in S^{(k)}} I_j \tag{2}$$

and the characteristic band subset is thus updated as follows:

$$S^{(k+1)} = S^{(k)} - \{x_r\} \tag{3}$$

2.2.2. Extraction of Characteristic Bands Based on Multi-Criteria Decision Making

To further evaluate the spectral characteristics of the characteristic band subsets, five parameters—mutual information, the inverse coefficient of variation, information entropy, random forest importance, and redundancy—were selected as evaluation indicators from the perspectives of signal quality, mutual information, information richness, feature contribution, and redundancy. A multi-criteria evaluation matrix was constructed, and the TOPSIS was employed to calculate the comprehensive relative closeness of characteristic bands to SOC. Specifically, the procedure was as follows:

1. The inverse coefficient of variation (ICV) of reflectance was used to measure the relative dispersion of a spectral signal and was defined as follows:

$$\mathrm{ICV}_j = \frac{\mu_j}{\sigma_j + \varepsilon} \tag{4}$$

where μ_j and σ_j represent the mean and standard deviation of the reflectance at the j band, respectively, and ε is a small value introduced to prevent the denominator from being zero. A higher ICV value indicates that the relative variability of reflectance in this waveband is lower.

2. Mutual information (MI) was used to measure the nonlinear dependence between the candidate bands and SOC and was expressed as follows:

$$MI\left(x_j, y\right) = \iint p\left(x_j, y\right) \ln \frac{p\left(x_j, y\right)}{p\left(x_j\right) p(y)} dx_j dy \tag{5}$$

where x_j represents the spectral reflectance of the j band and y represents the measured SOC content. Here, $p(\cdot)$ represents the probability density function, $p(x_j)$ and $p(y)$ represent the marginal probability density functions of the reflectance of the y spectral band and the measured SOC content, respectively, and $p(x_j, y)$ represents their two-dimensional joint probability density function. A higher mutual information value indicates that the corresponding band contains more SOC-related information.

3. Information entropy was used to quantify the amount of information contained in each spectral band and is given as follows:

$$H_j = -\sum_k h_{jk} \ln h_{jk} \tag{6}$$

where h_{jk} represents the probability distribution of the reflectance of the j band. Higher information entropy indicates that the corresponding band contains richer spectral information.

4. Random forest (RF) importance was used to quantify the contribution of each band to the SOC prediction accuracy in the random forest model. The importance of the j band (I_j) can be expressed as follows:

$$I_j = \sum_{t=1}^{T} \sum_{s \in S(j,t)} \Delta I(s,t) \tag{7}$$

where T represents the total number of decision trees in the random forest, $S(j, t)$ represents the set of splits associated with the j band in the t decision tree, and $\Delta I(s, t)$ represents the reduction in impurities resulting from the split using the j band. A higher random forest importance value indicates the greater contribution of the corresponding band to the prediction results of the RF model.

5. Redundancy was used to measure the independence of one band from the other spectral bands and is given as follows:

$$R_j = \frac{1}{m-1} \sum_{k \neq j} \left|\mathrm{Corr}\left(x_j, x_k\right)\right| \tag{8}$$

where m represents the total number of candidate bands and Corr (x_j, x_k) represents the correlation coefficient between the j and k bands. A lower redundancy value indicates weaker correlations between the corresponding band and the other bands and thus higher independence.

Suppose that m preliminary characteristic band subsets were obtained after RFE and n evaluation indicators were considered. Taking each band as an evaluation object, the values

of the corresponding evaluation indicators were calculated for each band, and the original evaluation matrix ($\boldsymbol{X}$) was constructed as follows:

$$\boldsymbol{X} = \begin{bmatrix} x_{11} & x_{12} & \cdots & x_{1n} \\ x_{21} & x_{22} & \cdots & x_{2n} \\ \vdots & \vdots & \ddots & \vdots \\ x_{m1} & x_{m2} & \cdots & x_{mn} \end{bmatrix} \tag{9}$$

The original matrix ($\boldsymbol{X}$) was normalized to eliminate the differences in dimensionality among the evaluation indicators. The evaluation indicators were divided into benefit-type and cost-type indicators.

For benefit-type indicators, the normalized value (η_{ij}) was calculated as follows:

$$\eta_{ij} = \frac{x_{ij} - \min_i x_{ij}}{\max_i x_{ij} - \min_i x_{ij}} \tag{10}$$

For cost-type indicators, the normalized value (η_{ij}) was calculated as follows:

$$\eta_{ij} = \frac{\max_i x_{ij} - x_{ij}}{\max_i x_{ij} - \min_i x_{ij}} \tag{11}$$

where $\max_i x_{ij}$ and $\min_i x_{ij}$ represent the maximum and minimum values of the j evaluation indicator among all candidate bands, respectively. After normalization, $\eta_{ij} \in [0, 1]$, and the normalized matrix ($\eta = (\eta_{ij})$) was obtained.

The weights of the evaluation indicators were determined using the entropy weight method. It is an objective weighting approach based on information entropy and the degree of dispersion in indicator data. After normalization of the original data matrix, the normalized values were multiplied by the corresponding indicator weights (w_j) to establish the weighted normalized matrix (V), which was expressed as follows:

$$V = \begin{bmatrix} v_{11} & v_{12} & \cdots & v_{1n} \\ v_{21} & v_{22} & \cdots & v_{2n} \\ \vdots & \vdots & \ddots & \vdots \\ v_{m1} & v_{m2} & \cdots & v_{mn} \end{bmatrix} \tag{12}$$

v_{ij} was expressed as follows:

$$v_{ij} = w_j \cdot \eta_{ij} \tag{13}$$

Subsequently, the positive and negative ideal solutions (v_j^+ and v_j^-) were determined. The positive ideal solution was composed of the optimal values of each evaluation indicator, whereas the negative ideal solution was composed of the worst values.

The Euclidean distances to the positive and negative ideal solutions (D_i^+ and D_i^-) could be further obtained as follows:

$$D_i^+ = \left(\sum_{j=1}^{n} \left(v_{ij} - v_j^+ \right)^2 \right)^{\frac{1}{2}}, i = 1, 2, \cdots, m \tag{14}$$

$$D_i^- = \left(\sum_{j=1}^{n} \left(v_{ij} - v_j^- \right)^2 \right)^{\frac{1}{2}}, i = 1, 2, \cdots, m \tag{15}$$

Finally, the relative closeness (C_i) was calculated to evaluate the relative proximity of each candidate band to the positive and negative ideal solutions:

$$C_i = \frac{D_i^-}{D_i^+ + D_i^-} \quad (16)$$

The relative closeness quantitatively characterizes the proximity of each band to the positive and negative ideal solutions and can comprehensively reflect its overall performance under the multi-dimensional evaluation system. A higher relative closeness value indicates that the corresponding band is closer to the ideal evaluation state. According to the relative closeness values, all preliminary characteristic band subsets were ranked in descending order, and the bands with relatively high closeness values were selected as the spectral characteristic bands for SOC and were subsequently used for the model construction and SOC inversion analysis.

2.3. Modeling Methods and Evaluation Metrics

Previous hyperspectral remote sensing studies have employed nonlinear models for modeling, such as one-dimensional convolutional neural network (1D-CNN), back propagation neural network (BPNN), and support vector machine (SVM), and linear regression approaches such as partial least-squares regression (PLSR) are also used for inversions [27]. However, a single model often has difficulty simultaneously achieving high fitting and generalization capabilities and is prone to overfitting, underfitting, and insufficient model stability, thereby limiting further improvements in its prediction accuracy. In this study, a stacking ensemble regression model was employed to construct an ensemble prediction model. Stacking is a classical ensemble learning method, the core idea of which is to generate the prediction results of multiple base learners through cross-validation and to subsequently fuse these multi-source prediction results using a meta-learner to obtain the final prediction [28]. Compared with a single model, stacking can effectively integrate the advantages of different models, reduce model bias and variance, and enhance the fitting and generalization capabilities of the model for complex nonlinear relationships.

The performance of a stacking model depends not only on the prediction capabilities of individual base learners but also on their diversity and complementarity. In this study, 1D-CNN, XGBoost, SVR, and PLSR were selected as the base learners, while random forest (RF) was employed as the meta-learner. Specifically, the 1D-CNN can adaptively extract local and deep features from spectral data [29]; SVR maps spectral features into a high-dimensional space through kernel functions and can effectively capture the complex nonlinear relationships between SOC content and spectral reflectance; XGBoost provides strong representation capabilities for complex data through the training of multiple decision trees; PLSR is capable of handling high-dimensional collinearity among spectral data. These models differ substantially in their feature representation and modeling mechanisms, enabling them to characterize the complex relationships between SOC and hyperspectral features from different perspectives, and thus provide good complementarity. The flowchart of the stacking model is shown in Figure 6. First, five-fold cross-validation was performed on the training set to train each base learner and generate the corresponding out-of-fold (OOF) predictions. These OOF predictions were subsequently combined to form the meta-feature set, which was used to train a random forest (RF) meta-learner for final prediction. Thus, the proposed approach establishes a heterogeneous ensemble learning framework by integrating a deep learning model, traditional nonlinear machine learning models, and a linear statistical model, providing a foundation for high-precision SOC inversion.

To evaluate the prediction performance of the SOC inversion model, the coefficient of determination (R^2), root-mean-square error (RMSE), ratio of performance to deviation (RPD) and ratio of performance to interquartile range (RPIQ) were selected as evaluation metrics [30]. Among these metrics, the R^2 was used to characterize the degree of agreement between the predicted and measured values, and its value ranges from 0 to 1, with a

value closer to 1 indicating the stronger ability of the model to explain the variation in the samples. The RMSE reflects the dispersion of prediction errors, namely, the average distance between the measured and predicted values. A lower RMSE indicates higher prediction accuracy. The RPD is used to evaluate the prediction capability and stability of the model and is calculated as the ratio of the standard deviation of the validation set to the RMSE. Generally, a higher RPD indicates stronger resistance to interference and better generalization performance. The RPIQ is calculated as the ratio of the interquartile range (IQR) of the measured SOC values to the RMSE, where the IQR is defined as the difference between the 75th and 25th percentiles. A higher RPIQ indicates better prediction performance relative to the variability of the measured SOC values within the interquartile range. By considering these metrics together, the performance of the inversion model can be comprehensively evaluated from multiple aspects, including the model fitting capability, prediction error, and prediction stability.

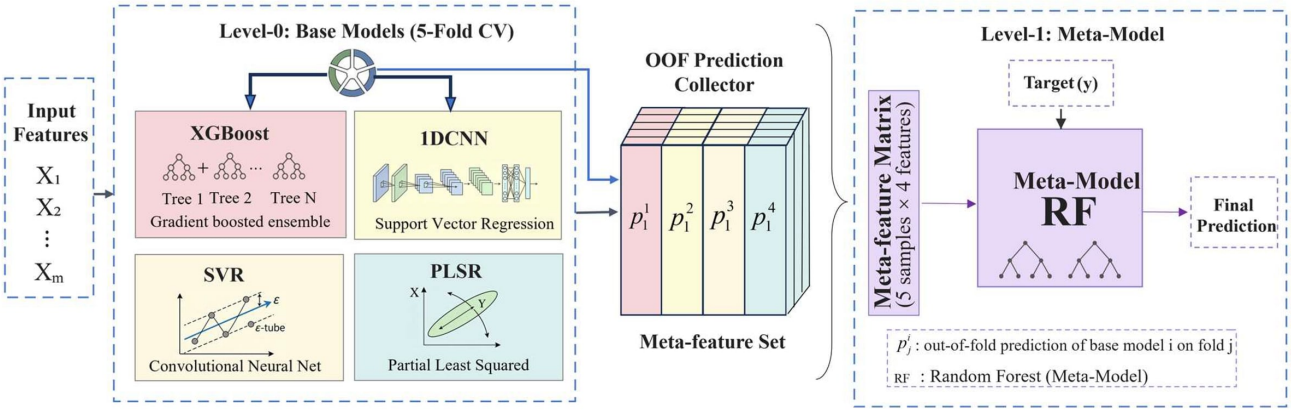


Figure 6. Schematic block diagram of stacking ensemble model.

3. Results

3.1. Characteristic Band Selection Using RFE–TOPSIS

Firstly, the XGBoost-based RFE method was applied to the SOC spectral reflectance data within the spectral range of 350–1002 nm. The XGBoost model was configured with 300 boosting trees, and Gain was used to evaluate feature importance. Five-fold cross-validation was performed using RMSE as the evaluation metric. One feature was removed at each iteration, with a minimum of five features retained. The optimal number of bands was determined based on the lowest mean cross-validation RMSE. A total of 19 preliminary characteristic band subsets were obtained, as shown in Figure 7: 402, 414, 454, 514, 566, 778, 794, 806, 838, 854, 886, 898, 914, 926, 938, 954, 970, 982, and 994 nm. In terms of spectral positions, the preliminary characteristic band subsets span both the visible and near-infrared regions.

The 19 preliminary characteristic band subsets were further evaluated by using the ICV, RF-Importance, Entropy, MI, and anti-redundancy. These indicators were used to comprehensively evaluate the relative variability of reflectance, feature contribution, information richness, and variable correlation. The normalized values of the individual indicators are shown in Figure 8. The distributions of the evaluation indicators across different spectral bands had substantial differences. For example, for the 514 nm band, the RF-Importance reached the highest value of 0.99, as indicated by the orange segment in the figure, and the corresponding Entropy, MI, ICV, and anti-redundancy values also remained relatively high, reaching 0.60, 0.59, in terms of the model contribution and overall performance. For the 926 nm band, Entropy reached the highest value (0.94), and MI and ICV were approximately

0.60, indicating abundant spectral information and a relatively strong association with SOC; in contrast, both RF-Importance and anti-redundancy were below 0.20, reflecting limited independent contribution and substantial overlap with neighboring bands. In comparison, although the 994 nm band also exhibited relatively higher Entropy, its ICV, MI, and RF-Importance values were all substantially lower than 0.10, suggesting that the band provided limited SOC-related information and contributed relatively little to model prediction. By integrating these evaluation criteria, the multi-criteria decision making is aimed to reduce the limitations of relying on a single criterion, rather than treating all indicators as direct measures of SOC relevance.

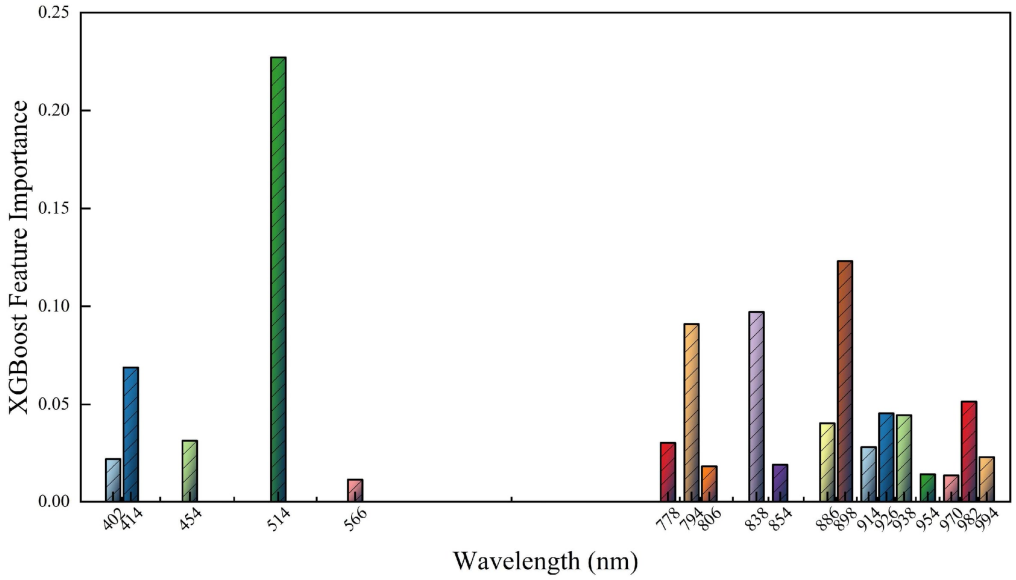


Figure 7. Characteristic band subsets selected via RFE.

The weights of the five evaluation indicators were determined using the entropy weight method rather than being manually assigned. The resulting weights primarily reflected the degree of variation among the evaluation indicators in the present dataset, rather than their direct associations with SOC or contributions to model prediction. Figure 9 shows the weights. Among the five indicators, RF-Importance received the highest weight of 0.3478, followed by anti-redundancy 0.2756. The weights of ICV, MI, and Entropy were 0.1514, 0.1192, and 0.1059, respectively. These weights were subsequently incorporated into the TOPSIS framework to comprehensively rank the candidate spectral bands.

According to the results of MI, RF importance, and other indicators (Figure 8), the value distributions and differences were further analyzed to determine the weights of the evaluation indicators. These weights were then incorporated into the TOPSIS comprehensive evaluation process to calculate the relative closeness of each candidate band. Figure 10 presents the comprehensive ranking results based on the TOPSIS relative closeness. The individual bands exhibited different overall performances across the multiple evaluation indicators, resulting in substantial differences in their relative closeness values, ranging from 0.2 to 0.7. To further reduce redundant information and improve prediction performance, a TOPSIS relative-closeness threshold was used to select spectral bands. The threshold was not fixed a priori; instead, it was selected exclusively within the training set by scanning values from 0.2 to 0.4 in steps of 0.05 and comparing the number of retained bands against model performance. The validation set was held out throughout this procedure and did not participate in threshold selection. A value of 0.3 provided a better trade-off between feature parsimony and accuracy; a lower threshold of 0.25 retained 15 bands but reduced performance. Accordingly, 12 spectral bands (402, 414, 454, 514, 778, 794, 838, 886, 898, 926,

938, and 954 nm) with relative closeness values >0.3 were selected for SOC prediction in this dataset. Among them, the 514 nm band exhibited the highest relative closeness of 0.707, indicating its superior overall performance across the multiple evaluation indicators. The 402, 414, 838, and 898 nm bands also exhibited relatively high relative closeness values of approximately 0.45, indicating strong comprehensive information representation capabilities and good correlations with SOC contents. These bands could effectively characterize the SOC effects on the spectral reflectance. For bands near the threshold, the relative closeness values at 806 and 854 nm were 0.297 and 0.272, respectively, both below the 0.30 threshold; whereas those at 886 and 778 nm were 0.318 and 0.321, respectively, both above the threshold. Although these values were relatively close to the threshold, the retention or removal of these bands was determined by the predefined threshold rule. In contrast, the 994 nm band did not reach the selection threshold, revealing that the TOPSIS can comprehensively consider multiple evaluation indicators and avoid mis-selection caused by an outstanding performance in a single indicator.

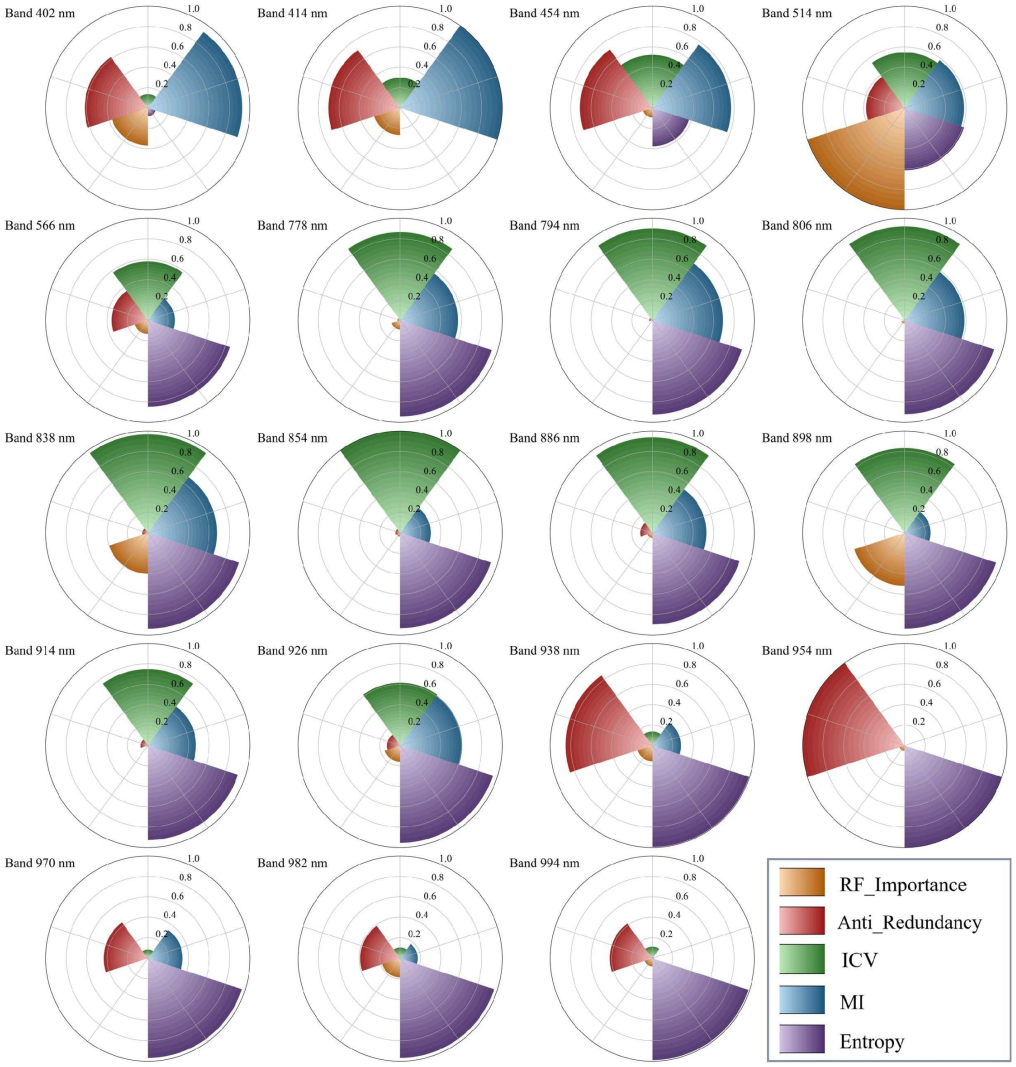


Figure 8. Evaluation indicators of 19 spectral characteristic bands.

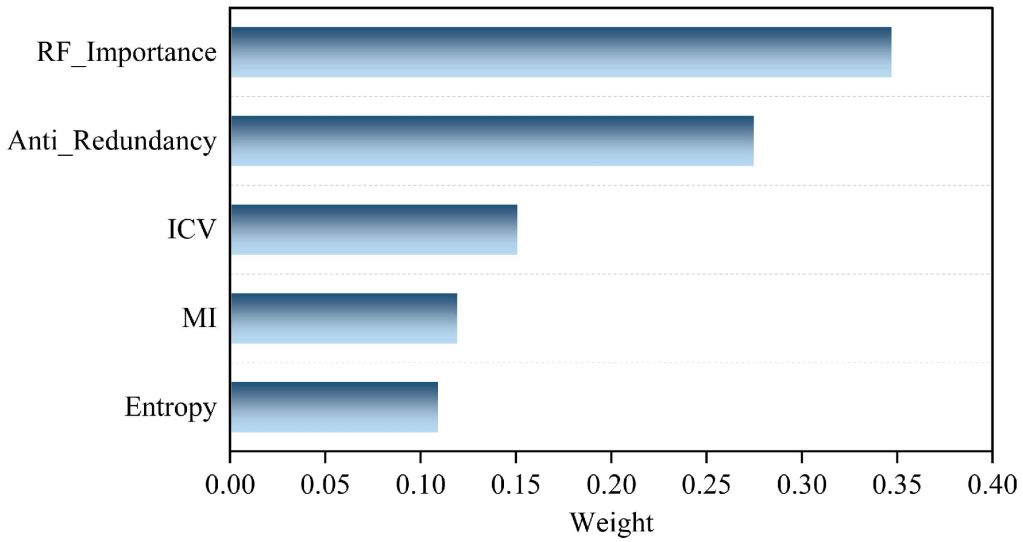


Figure 9. The weights of each indicator.

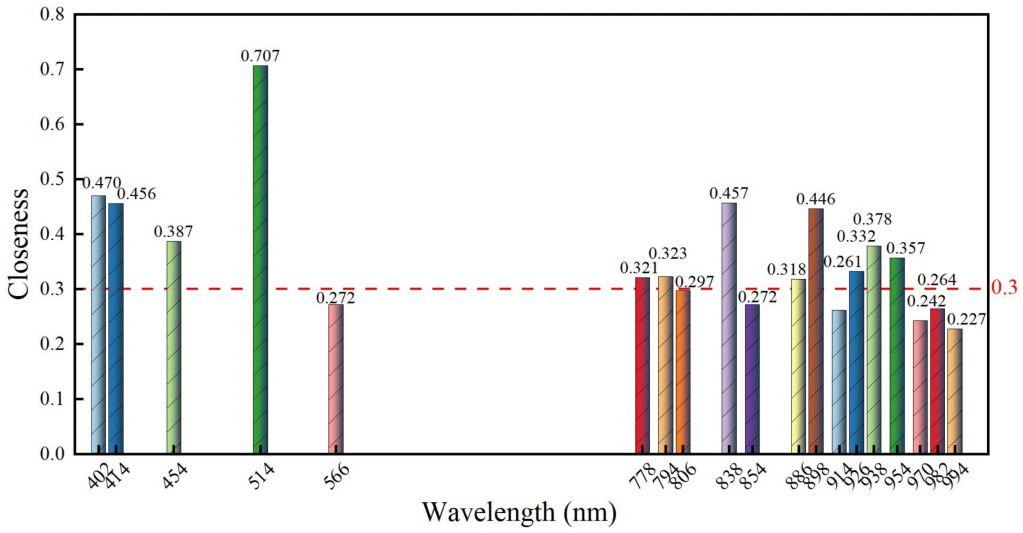


Figure 10. Closeness degrees of optimal bands based on TOPSIS.

3.2. SOC Estimation and Analysis

A stacking ensemble regression model was constructed for training to verify the effectiveness of the XGBoost-based RFE spectral characteristic band selection method, with the 1D-CNN, XGBoost, SVR, and PLSR selected as the base learners and RF employed as the meta-learner, at integrating the learning results of the base models. First, the samples were divided into training and validation sets. During the training, the hyperparameters of each base learner were optimized. Bayesian optimization was employed to search for the optimal hyperparameter combinations of XGBoost and SVR, a grid search was used to determine the optimal number of principal components for PLSR, and comparative experiments were conducted to optimize the network structure and training hyperparameters of the 1D-CNN.

The optimized parameters are listed in Table 2. The 1D CNN consisted of two one-dimensional convolutional layers, Conv1D (64, 3) and Conv1D (128, 3), which contained 64 and 128 convolution kernels with a kernel size of 3, respectively, to extract local features from the spectral sequences. Each convolutional layer was followed by a max-pooling layer with a pool size of 2. The network then included two fully connected layers with 256 and 128 neurons, respectively, both using the rectified linear unit (ReLU) activation function. A dropout layer with a dropout rate of 0.2 was applied after each fully connected

layer. The output layer consisted of a single neuron with linear activation to predict SOC content. The model was trained using the mean squared error (MSE) loss function and the Adam optimizer with a fixed learning rate of 0.0005, a batch size of 4, and 100 epochs. For the XGBoost, the maximum depth of the decision trees was set to 6, the learning rate was 0.05, the number of estimators was 114, the subsample ratio was 0.7, and the L1 and L2 regularization coefficients were 4.169 and 2.925, respectively. The radial basis function (RBF) kernel for nonlinear fitting was employed for the SVR, with a penalty coefficient (C) of 14.04 and a kernel coefficient gamma of 0.293. The optimal number of principal components for the PLSR was 3.

Table 2. Parameters of each base model.

Model	Parameters
1D-CNN	Conv1D(64,3)-MaxPool(2)-Conv1D(128,3)-MaxPool(2)-Dense(256)-Dense(128), Dropout = 0.2, Adam(learning_rate = 0.0005)
XGBoost	max_depth = 6, learning_rate = 0.05, n_estimators = 114, subsample = 0.7, reg_alpha = 4.169, reg_lambda = 2.925
SVR	kernel = RBF, C = 14.04, gamma = 0.293, epsilon = 0.190
PLSR	n_components = 3

SOC inversion results were obtained using the 12 selected spectral bands as the input of the stacking model and are shown in Figure 11. Figure 11a,b correspond to the training and validation sets, respectively. The coefficients of determination (R^2) for the training and validation sets reached 0.96 and 0.85, respectively, while the RMSE values were 0.50 and 0.96 g/kg, respectively, and the RPD values were 5.58 and 2.47, respectively, indicating that the model achieved a high fitting accuracy and good generalization capability. Both datasets were distributed around the 1:1 reference line, indicating that the model could accurately predict SOC contents without obvious systematic over- or underestimation. The marginal distributions of the training and validation sets are also presented in Figure 11. The upper histograms show the frequency distributions of the measured and predicted SOC values. The measured and predicted SOC values in both the training and validation sets were mainly concentrated in the range of 7–12 g/kg, and the frequency distributions and kernel density curves of the two datasets exhibited generally consistent patterns, indicating good distribution consistency between the training and validation sets.

Figure 12 presents the violin plots of the prediction residuals for the training and validation sets, where the white squares represent the mean values, and the white squares indicate the mean residual values, and the circles represent the individual prediction residuals in each set. The residuals of the training set were mainly concentrated around zero, and most samples were distributed within the range of −0.5 to 0.5 g/kg. The residual range of the validation set was slightly wider, and the overall violin distribution was relatively longer. Overall, neither group of residuals exhibited obvious systematic shifts or abnormal distributions, indicating relatively small prediction errors and the good generalization ability and stability of the model.

The Pearson correlation coefficients between the OOF errors of different models were calculated and a correlation heatmap was generated to analyze the complementary performances of the individual base learners. OOF-Res denotes the out-of-fold residual, defined as the difference between the measured SOC value and the corresponding OOF prediction generated by each base learner during five-fold cross-validation. Lower residual correlation coefficients indicate greater differences in the error variation patterns among models, suggesting potentially stronger predictive complementarity, whereas higher residual correlation

coefficients indicate more similar trends in prediction errors across different models. As shown in Figure 13, the error patterns among the different base models had significant differences. The error correlation between the 1D-CNN and PLSR was the lowest, with a coefficient of 0.368. The error correlation coefficients between the 1D-CNN and XGBoost and SVR were 0.559 and 0.590, respectively, and the corresponding coefficients between PLSR and XGBoost and SVR were 0.745 and 0.697, respectively. XGBoost and SVR exhibited the highest error correlation, with a coefficient of 0.856. These results indicate that the responses of the different base learners to sample prediction errors varied considerably. In particular, the 1D-CNN and PLSR exhibited strong error complementarity, whereas XGBoost and SVR showed relatively consistent error variation patterns. This error complementarity provides a rationale for constructing a stacking model, as combining base learners with diverse error patterns may enable the meta-learner to exploit complementary predictive information and improve the overall prediction performance [31,32]. The differences in error correlations among the models were mainly attributed to their different modeling mechanisms and feature representation approaches. The 1D-CNN extracts local spectral features and deep nonlinear features, whereas PLSR mainly utilizes the linear relationships between the spectral variables and SOC, resulting in substantially different error patterns between the two models. In contrast, both XGBoost and SVR have strong nonlinear fitting capabilities, and their learning mechanisms for data features are relatively similar, leading to a higher error correlation.

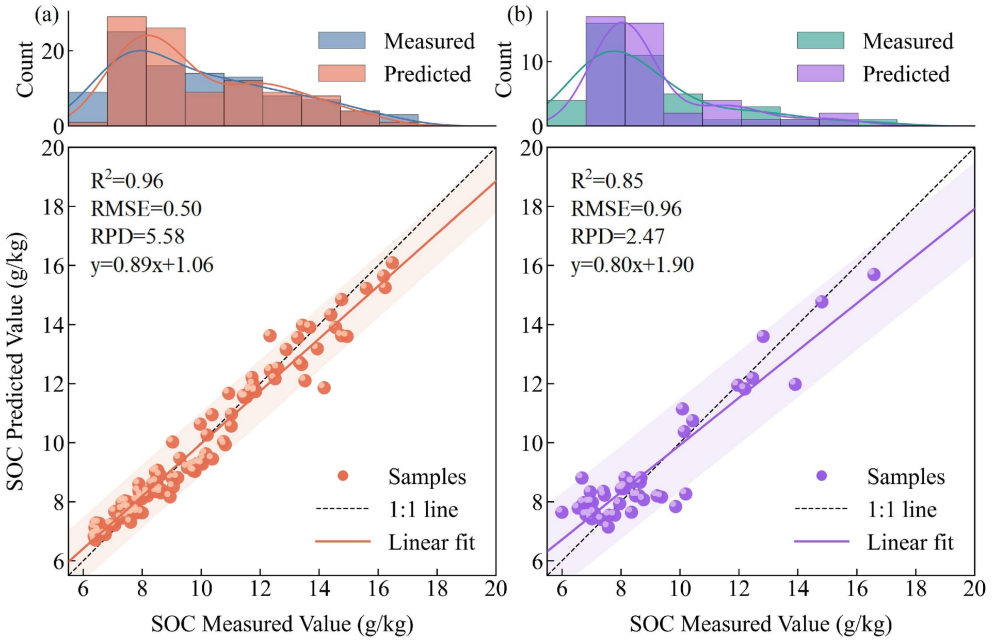


Figure 11. RFE–TOPSIS–stacking model prediction results: (**a**) training set; (**b**) validation set.

Furthermore, the SOC prediction performance of the stacking ensemble model was compared with those of the four individual machine learning models (SVR, the 1D-CNN, XGBoost, and PLSR), and the R^2, RMSE, RPD, and RPIQ values for both the training and validation sets were evaluated, as shown in Figure 14. The stacking model achieved the highest R^2, RPD and RPIQ on both the training and validation sets. For the validation set, the stacking model achieved the highest R^2 (0.85), RPD (2.47), and RPIQ (2.72), as well as the lowest RMSE (0.96 g/kg). By comparison, the nonlinear models-SVR, the 1D-CNN, and XGBoost obtained R^2 values of 0.77, 0.78, and 0.71, respectively, with validation. The linear PLSR model showed a relatively lower R^2 (0.37). These results indicate that by combining

linear and nonlinear models in the proposed stacked ensemble, the complementary model learning capabilities of both can be fully exploited.

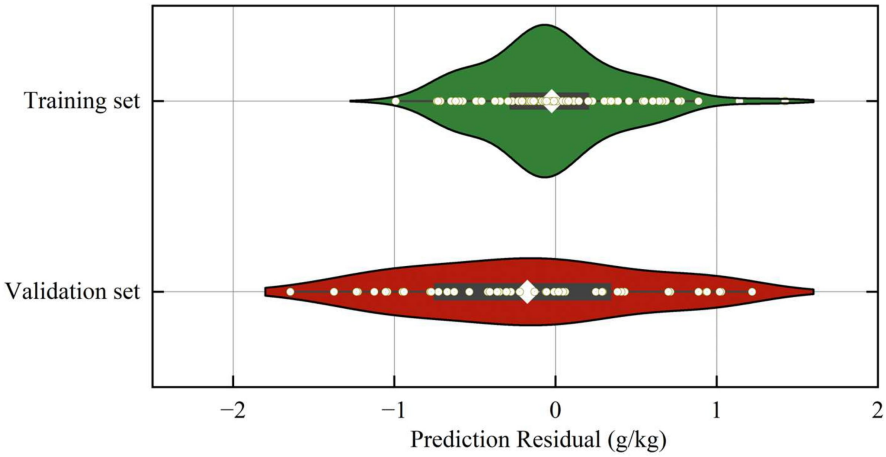


Figure 12. Residual distributions of measured and predicted values for training and validation sets.

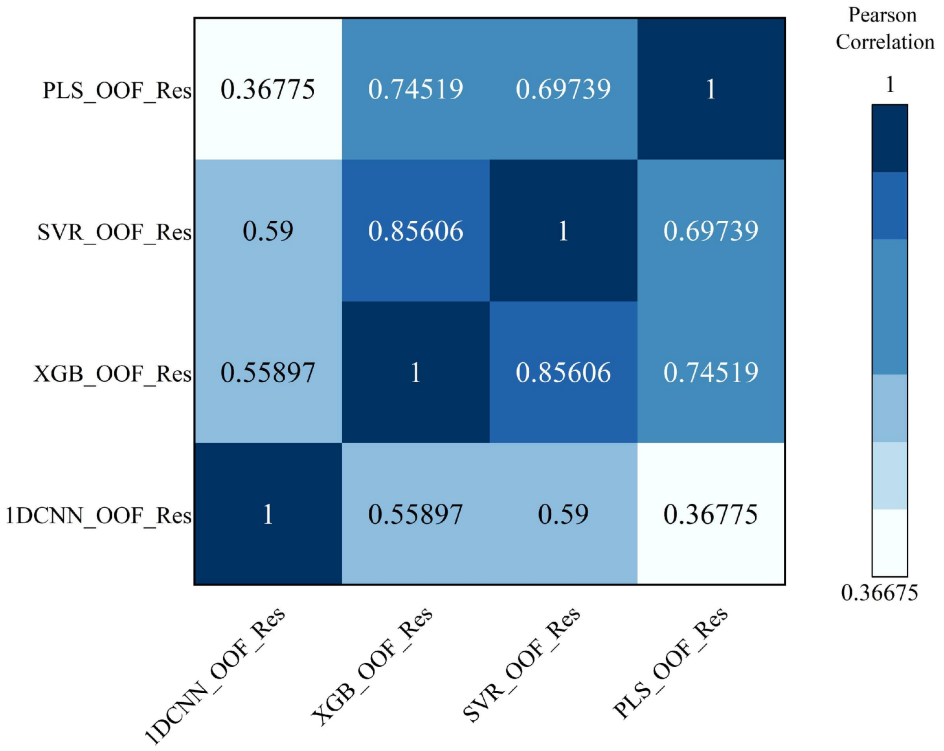


Figure 13. Heatmap of OOF error correlation coefficients among base models.

From the perspective of model composition, the stacking ensemble system established in this study integrates a deep learning model, nonlinear machine learning models, and a linear statistical model, forming a relatively reasonable heterogeneous ensemble structure. The base learners exhibited good error complementarity, providing a solid foundation for the meta-learner to integrate the advantages of different models. This structure facilitates the characterization of the complex relationships between SOC and hyperspectral features from different perspectives, thereby further improving the inversion accuracy and generalization capability of the SOC prediction model.

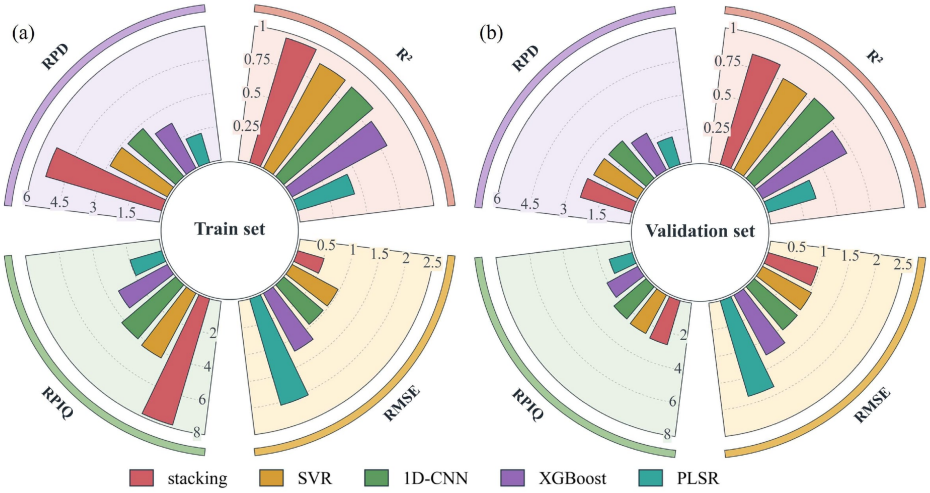


Figure 14. Comparison of prediction performances of different models: (**a**) training set; (**b**) validation set.

3.3. Mapping of Soil Organic Carbon

Furthermore, the proposed RFE-TOPSIS-stacking model was applied to the entire UAV hyperspectral image to perform pixel-level SOC estimation and generate SOC spatial distribution maps, thereby providing an application example of the constructed prediction model. The predicted SOC results were classified and mapped using the one-third standard deviation classification method in ArcMap (10.8). The spatial distribution maps of the SOC contents for areas A, B, and C were obtained and are shown in Figures 15–17.

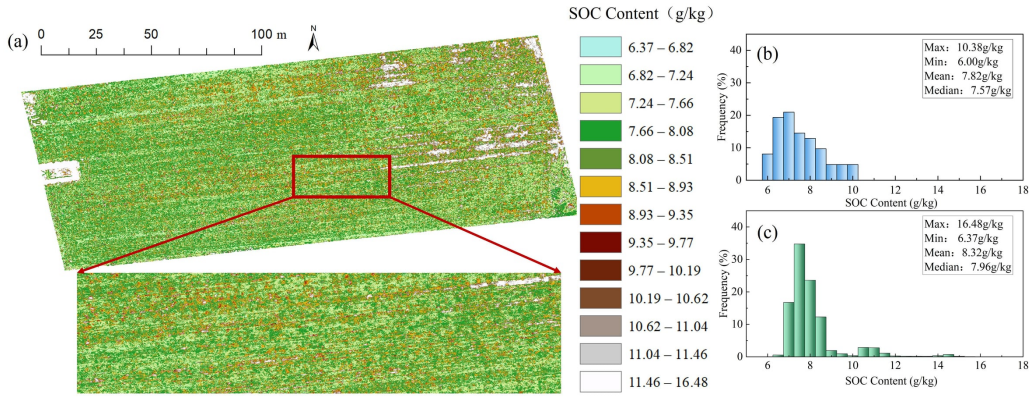


Figure 15. Spatial distribution map and histogram of SOC content in study area A: (**a**) spatial distribution; (**b**) histogram of SOC content at sampling sites; (**c**) histogram of per-pixel predicted SOC content.

Figure 15 presents the spatial distribution and analysis of the SOC contents in area A. As shown in Figure 15a, the spatial distribution of the SOC was relatively uniform, exhibiting an interwoven texture of east–west-oriented stripes and patches. Here, the 10th to 90th percentile range (P10–P90) was used to characterize the main distribution of predicted SOC values in each study area. In terms of the predicted SOC values, the SOC contents of the valid pixels were mainly distributed within the range of 7.37–9.59 g/kg, indicating that the overall SOC content in the study area was moderate. An enlarged view of the local area is also provided in the left panel, showing relatively continuous and smooth spatial variations in the SOC. The local red region had an SOC content of approximately 9.50 g/kg and corresponded to the ridge tops of the farmland, which might be related to the relatively high accumulation of crops and root and crop residues on the ridge tops. Moreover, the statistical histograms of the measured and predicted SOC values at the sampling points

were analyzed and are shown in Figure 15b,c. Both the measured and predicted SOC values were mainly concentrated in the range of 7–9 g/kg, and their concentration ranges and overall distribution patterns were generally consistent.

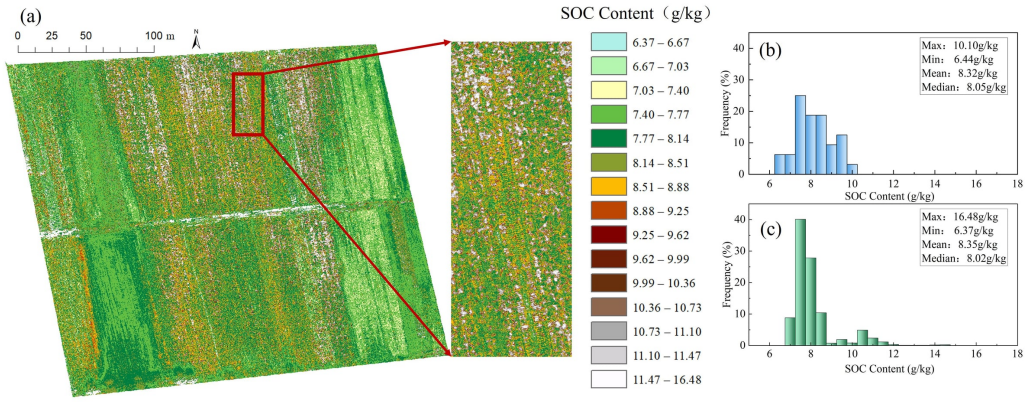


Figure 16. Spatial distribution map and histogram of SOC content in study area B: (**a**) spatial distribution; (**b**) histogram of SOC content at sampling sites; (**c**) histogram of per-pixel predicted SOC content.

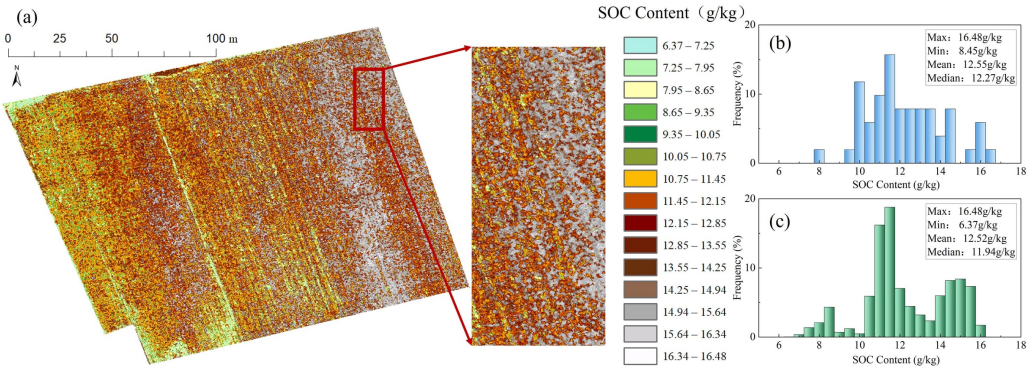


Figure 17. Spatial distribution map and histogram of SOC content in study area C: (**a**) spatial distribution; (**b**) histogram of SOC content at sampling sites; (**c**) histogram of per-pixel predicted SOC content.

Figure 16 presents the spatial distribution of the SOC contents in area B. The overall SOC content level in area B was comparable to that in area A, the predicted SOC values of the valid pixels were primarily concentrated between 7.52 and 11.01 g/kg. The high- and low-value areas were continuously distributed along the direction of the farmland ridges. Figure 16b,c present the statistical histograms of the measured and predicted SOC values. The mean measured SOC content at the sampling points was 8.32 g/kg, while the mean predicted SOC content was 8.35 g/kg, a difference of only 0.03 g/kg, indicating that the model predictions could effectively preserve the overall statistical characteristics of the SOC.

The spatial distribution and analysis of the SOC contents in area C are displayed in Figure 17. As shown in Figure 17a, the spatial distribution of the SOC exhibited north–south-oriented stripe patterns. The predicted SOC values for the majority of valid pixels fell within the range of 9.98–15.43 g/kg, and high-value areas occupied the majority of the study area, while low-value areas were sporadically distributed along the edges and in the ridge-bottom regions in the central part of the study area. This pattern indicates that the spatial variation in the SOC has been jointly influenced by anthropogenic and natural factors, such as agricultural management practices and microtopography.

A comparison of the three study areas revealed that the SOC content in area C was approximately 4 g/kg higher than those in areas A and B. This difference might be associated with differences in cropping systems and farmland management practices [33]. On the one hand, vegetable crops generally have shorter growth cycles and can provide more root residues and organic matter to the soil during growth, thereby providing an important source for SOC accumulation. On the other hand, relatively large amounts of organic fertilizer are often applied during vegetable production to ensure crop yields and quality, which may further increase SOC contents. In contrast, wheat–maize rotation areas are mainly used for grain production and have relatively simple crop structures; thus, the sources of soil organic matter input are relatively limited, resulting in a comparatively lower rate of SOC accumulation.

To further evaluate the prediction accuracy of the model, predicted SOC values were extracted from the generated maps at the coordinates of the 44 independent validation samples, which contained no training samples, and compared with the corresponding measured SOC values, as shown in Figure 18. The upper panels compare the measured and predicted values, indicating that the predictions generally followed the variation patterns of the measurements. The lower panels present the prediction residuals and corresponding relative errors. The model exhibited generally small errors: most validation sampling points had absolute residuals below 1 g/kg, with a maximum absolute residual of 1.65 g/kg; approximately 80% had relative errors within ±10%. Only a few sampling points exhibited relatively large errors, indicating relatively high overall prediction accuracy.

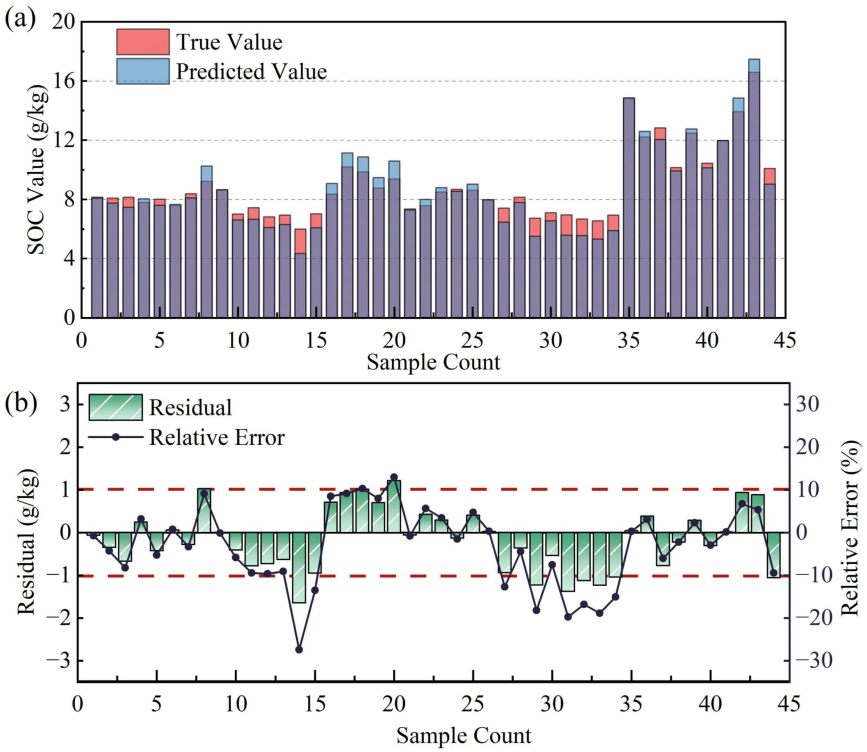


Figure 18. Analysis of SOC errors of 44 validation sample points extracted based on hyperspectral image inversion results: (**a**) true and predicted values; (**b**) residual and relative errors.The purple regions in the bar chart result from the overlap between the red and blue bars.

4. Discussion

4.1. Comparison of Different Feature Selection Strategies

As is well known, redundant information in hyperspectral data might increase model complexity and affect prediction performance; thus, an appropriate feature selection strategy

is an important key to improve SOC prediction performance [34,35]. We further analyzed the results of the full-band (164 bands) baseline models, including RF and PLSR. Before model training, first-order derivative transformation was applied to the spectral data comprising all 164 bands. The results are shown in Figure 19. When all 164 bands were used as model inputs, the stacking model achieved an R^2 of 0.54, an RMSE of 1.48 g/kg, and an RPD of 1.60 on the validation set, outperforming both RF and PLSR. The RF and PLSR models achieved R^2 values of 0.48 and 0.43, respectively, with corresponding RMSE values of 1.57 g/kg and 1.64 g/kg.

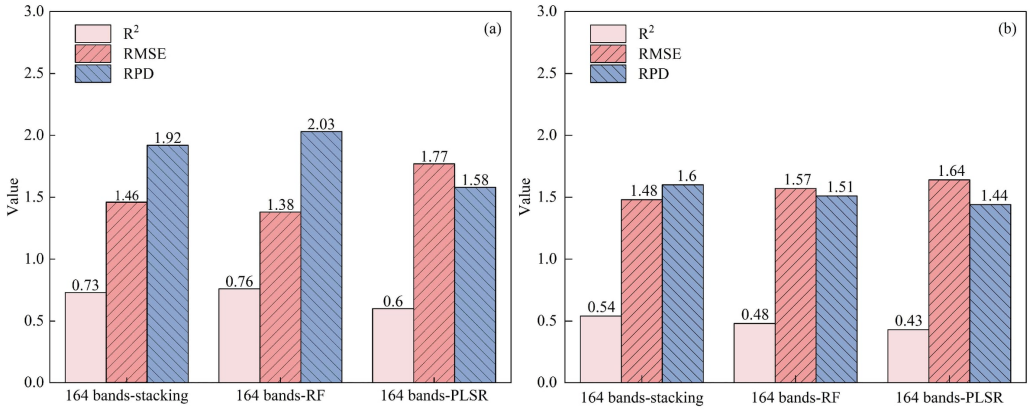


Figure 19. Predictive capabilities of different models for soil organic carbon based on entire spectral range: (**a**) training set; (**b**) validation set.

Furthermore, ablation experiments were conducted to investigate the effects of spectral feature selection on the SOC prediction performance using different feature selection methods, including RFE, MI, competitive adaptive reweighted sampling (CARS) [36] and Spectral Profile Analysis (SPA). The results are shown in Figure 19. Using the traditional RFE method, 19 characteristic bands were selected (Figure 7) and used as inputs to the stacking model. The results shown in Figure 20a,a′ correspond to the training and validation sets, respectively. The validation set achieved an R^2 of 0.68 and an RMSE of 1.24 g/kg, which were notably inferior to the results obtained using the RFE–TOPSIS method (R^2 = 0.85 and RMSE = 0.96 g/kg; Figure 11). Using the traditional MI method, 20 characteristic bands were selected, yielding an R^2 of 0.61 and an RMSE of 1.38 g/kg on the validation set. When CARS was used for feature selection, 23 bands distributed across 430–986 nm were obtained and used as inputs to the stacking model, resulting in R^2 values of 0.83 and 0.60 on the training and validation sets, respectively. When the SPA method was used and 24 characteristic bands were selected, the R^2 and RMSE on the validation set were 0.70 and 1.22 respectively. Thus, for the present dataset, the characteristic bands selected via the proposed RFE–TOPSIS method exhibited superior prediction performances. This may be attributed to the fact that TOPSIS comprehensively evaluates candidate bands from five aspects: signal quality, mutual information, information richness, feature contribution, and redundancy. Compared with traditional methods based on a single criterion, this multi-criteria approach provides a more comprehensive and balanced evaluation of candidate bands. In addition, the two-stage RFE-TOPSIS framework balances computational efficiency and selection accuracy. RFE first performs preliminary screening to reduce the candidate feature space, followed by TOPSIS for further comprehensive evaluation, allowing the final bands to be selected based on their overall performance rather than solely on model-driven importance. Taken together, these results demonstrate that SOC prediction performance depends on both the choice of regression model and the composition of the input spectral features.

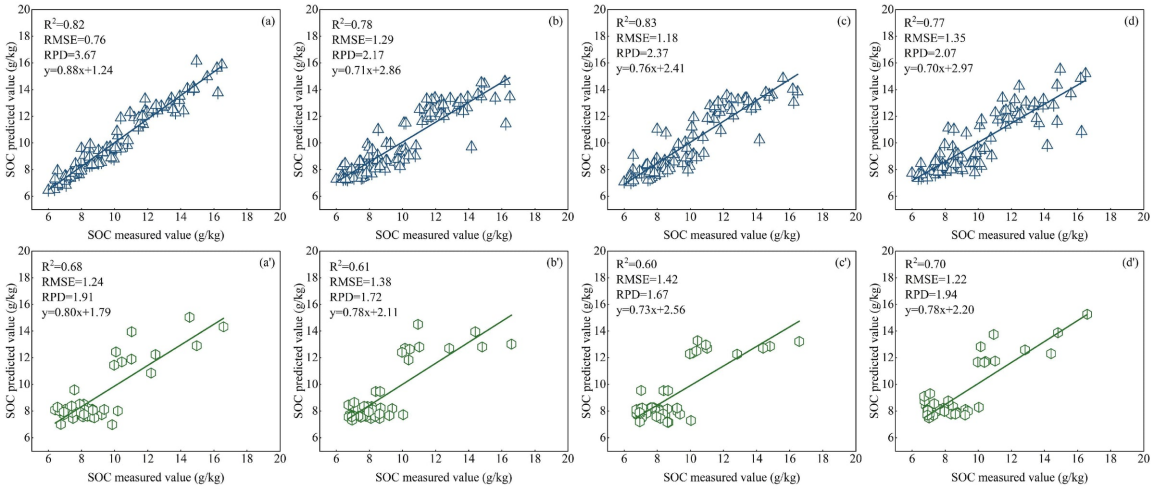


Figure 20. Comparison of training-set (**a**–**d**) and validation-set (**a′**–**d′**) results of stacking model under four feature band extraction methods: (**a**,**a′**) RFE; (**b**,**b′**) MI; (**c**,**c′**) CARS; (**d**,**d′**) SPA.

4.2. Different Meta-Learner Selection on Stacking Performance

To examine the effect of meta-learner selection, an ablation experiment was further conducted, in which the RF meta-learner was compared with simple averaging and ridge regression while keeping the base learners unchanged. Figure 21 shows the results: panels (a) and (a′) present the training and validation results for simple averaging, respectively, while panels (b) and (b′) present those for ridge regression. On the validation set, simple averaging yielded an R^2 of 0.67, an RMSE of 1.32 g/kg, and an RPD of 1.80; compared with 0.75, 1.24 g/kg, and 1.91 for ridge regression. Both alternatives These results are inferior to those by RF meta-learner (R^2 = 0.85, RMSE = 0.96 g/kg, and RPD = 2.47). This result indicates that RF integrates the base-learner predictions more effectively, which supports its adoption as the meta-learner in the Stacking model.

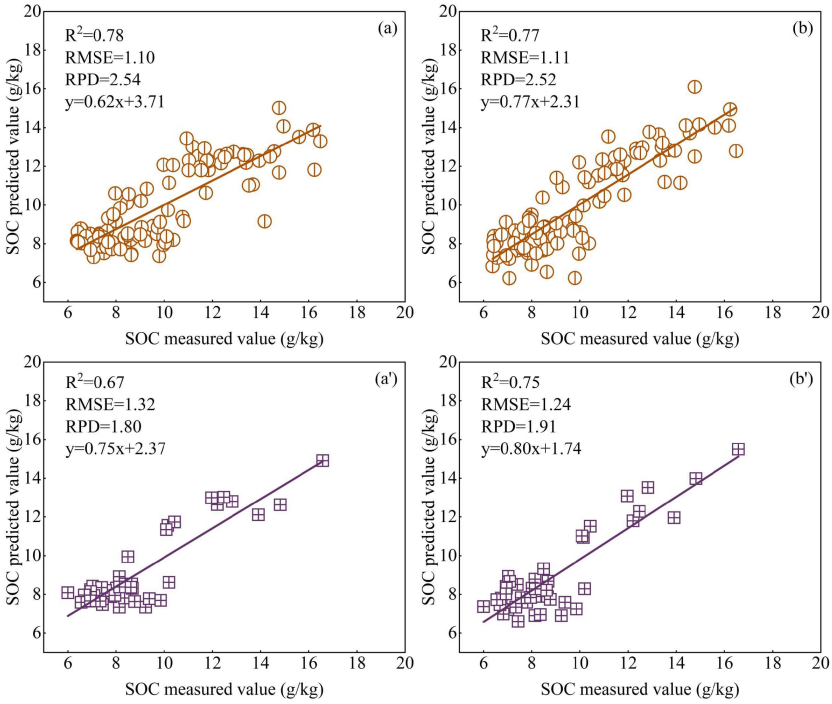


Figure 21. The prediction results of different meta-learners on the training set (**a**,**b**) and the validation set (**a′**,**b′**): (**a**,**a′**) averaging meta-learners; (**b**,**b′**) ridge meta-learners.

4.3. Feature Band Selection

In this study, 12 spectral bands (402, 414, 454, 514, 778, 794, 838, 886, 898, 926, 938, and 954 nm) were selected for SOC prediction. Notably, several selected bands are close to or fall within spectral regions previously associated with SOC. Alsaleh et al. reported associations between SOC and spectral reflectance at wavelengths of approximately 400, 530, 610, 800, 1000, and 1100 nm [37]. Similarly, Yang et al. identified SOC-related characteristic bands at 425–460 nm and 788–1195 nm [38]. This partial agreement with previous studies supports the plausibility of the selected bands for SOC prediction.

The selected bands span the visible and near-infrared (VNIR) regions, where spectral responses may be influenced by pigment absorption and molecular vibrations associated with soil organic matter, including vibrations involving C-H, N-H, and O-H bonds [39]. However, the specific contributions of these mechanisms to the selected bands cannot be established from the present analysis alone. In addition, VNIR reflectance is influenced by multiple soil properties, including iron oxide content, mineral composition, and soil moisture and texture, which affect spectral absorption and scattering and may contribute to indirect associations between reflectance and SOC [40,41]. Consequently, the selected bands may capture both SOC-associated spectral variations and indirect information related to other soil properties. As these potential intermediary factors were not independently evaluated in this study, their respective contributions remain uncertain and warrant further investigation.

4.4. The Relationship Between SOC and Soil Nutrients

To provide additional data support, we further analyzed the measured soil nutrient data, including total nitrogen (TN), available phosphorus (AP), and available potassium (AK). The radial bar charts in Figure 22 show the distribution of SOC and TN, AP, and AK contents across the three study areas, with Figure 22a corresponding to Areas A and B and Figure 22b corresponding to Area C. The mean contents of SOC, AK, AP, and TN in Areas A and B were 8.07 g/kg, 184 mg/kg, 30 mg/kg, and 0.11%, respectively, with relatively low values across all indicators. In contrast, the corresponding mean contents in Area C were 12.55 g/kg, 379 mg/kg, 75 mg/kg, and 0.17%, respectively. Area C exhibited higher soil nutrient contents, accompanied by a higher SOC content, indicating differences in SOC and soil nutrient levels among the study areas.

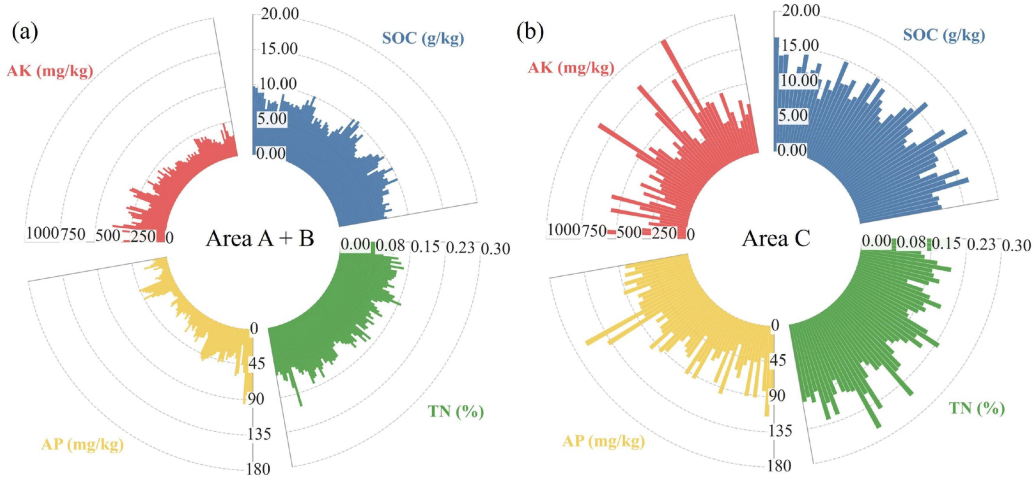


Figure 22. The differences in the contents of SOC, TN, AP, and AK between study area A + B and study area C. (**a**) area A + B; (**b**) area C.

Furthermore, Pearson correlation analysis was performed (Figure 23). The results showed that SOC was strongly positively correlated with TN (r = 0.93), AP (r = 0.82), and AK (r = 0.78). Meanwhile, TN, AP, and AK also exhibited significant positive correlations with one another, whereas pH showed relatively weak correlations with SOC and the other nutrient indicators. These results indicated positive statistical associations between SOC and soil nutrient contents in the present dataset.

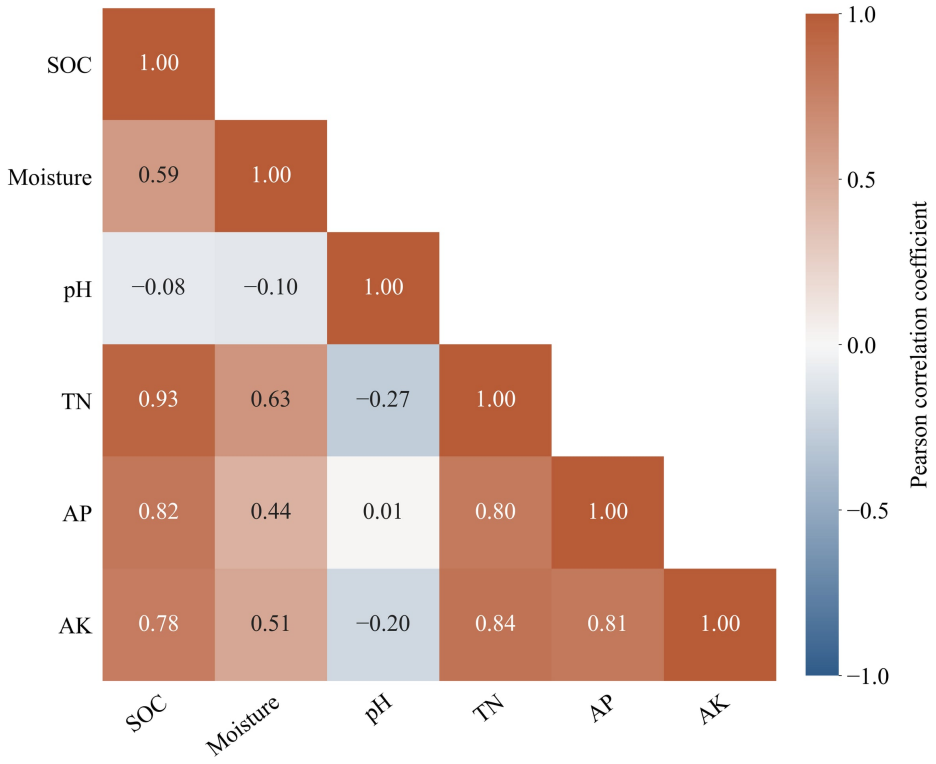


Figure 23. The correlation between SOC and other soil property contents.

4.5. Study Limitations and Future Work

This study has several limitations that should be considered when interpreting the results. First, the predictive performance of the proposed model was evaluated under the present dataset, sampling strategy, and data partitioning method. The limited sample size may compromise sample representativeness, and potential spatial autocorrelation among neighboring sampling locations may violate the independence assumption of model validation. Although the model achieved accurate field-scale SOC estimation under the current experimental conditions, it remains to be seen whether this performance can be extended to areas beyond the sampling coverage, and its generalization capability still awaits further verification. Future studies will increase the number of soil samples and expand their spatial coverage to improve representativeness, optimize the sampling design and data partitioning strategy to mitigate spatial autocorrelation. Also, more comprehensive cross-validation will be employed to assess model stability, and independent cross-area validation is conducted to evaluate generalization capability in unseen areas. Second, the SOC spatial distribution maps were generated primarily to demonstrate the application of the proposed method within the study areas and, in turn, to provide a preliminary check of the model's generalization capability through spatial extrapolation. Model prediction accuracy was assessed using 44 held-out validation samples; however, no spatially independent ground-truth samples were available to validate the mapping results. Future studies will therefore

incorporate additional such samples to further assess the accuracy and reliability of SOC spatial mapping.

5. Conclusions

Soil organic carbon (SOC) is an important indicator for assessing soil fertility, soil quality, and carbon cycling in agricultural ecosystems. UAV hyperspectral remote sensing provides high spatial resolution and abundant spectral information, enabling the rapid monitoring of SOC contents. However, hyperspectral data are characterized by high dimensionality, strong inter-band correlations, and substantial information redundancy. Therefore, spectral characteristic band selection is essential for improving the prediction accuracy and stability of SOC inversion models.

To address the problem of spectral feature redundancy, this study proposes a two-step progressive method for selecting hyperspectral characteristic bands of SOC by integrating RFE and the TOPSIS. First, the XGBoost-based RFE method was employed to preliminarily select characteristic band subsets from the original hyperspectral data, resulting in 19 spectral characteristic band subsets. Subsequently, the TOPSIS multi-criteria decision-making method was introduced to comprehensively evaluate the characteristic band subsets based on ICV, MI, Entropy, RF-Importance, and redundancy. The 19 characteristic band subsets were evaluated by closeness, and 12 optimal hyperspectral characteristic bands were selected for SOC prediction in the present dataset. Furthermore, a stacking-based SOC inversion model was constructed using a 1D-CNN, XGBoost, SVR, and PLSR as the base learners and RF as the meta-learner. The stacking model achieved R^2 values of 0.96 and 0.85 for the training and validation sets, respectively, demonstrating high SOC prediction accuracy and stability. The OOF error analysis revealed complementary information among the base models, which was effectively exploited by the stacking model to improve the SOC prediction performance. Compared with individual models such as SVR and the 1D-CNN, the stacking model achieved an R^2 of 0.85, an RMSE of 0.96 g/kg, and an RPD of 2.47 for the validation set, outperforming the individual model (1D-CNN: R^2 = 0.78, RMSE = 1.05 g/kg, and RPD = 2.19), indicating higher prediction accuracy with improved stability and generalization capability.

Based on the RFE–TOPSIS–stacking model established above, the model was further extended from the sample scale to the pixel-wise estimation of hyperspectral images, enabling the spatial representation of the SOC contents in the three study areas, A, B, and C. The obtained SOC mapping clearly revealed pronounced spatial heterogeneity, with the P10–P90 ranges of SOC being 7.37–9.59 g/kg in area A, 7.52–11.01 g/kg in area B, and 9.98–15.43 g/kg in area C. A point-by-point comparison of the measured and predicted SOC values for the validation samples showed that most absolute residuals were below 1 g/kg, with a maximum absolute residual of 1.65 g/kg, and approximately 80% had relative errors within ±10%, indicating good overall agreement between the predicted and measured SOC values. Overall, the proposed RFE–TOPSIS–stacking model enabled the selection of spectral characteristic bands from UAV hyperspectral data and achieved high-accuracy SOC inversion. The results provide technical support for rapid SOC monitoring using UAV hyperspectral remote sensing and provide a reference for the application of hyperspectral remote sensing in soil nutrient inversion and agricultural ecological monitoring.

Author Contributions: L.W.: Conceptualization, Investigation, Data curation, Formal analysis, Software, Visualization, Writing—review & editing, Writing—original draft. Y.W.: Conceptualization, Data curation, Formal analysis, Funding acquisition, Project administration, Investigation, Supervision, Writing—review & editing. K.L.: Data curation, Investigation, Methodology, Formal analysis, Writing—review & editing. N.L.: Data curation, Investigation, Formal analysis, Validation, Writing—review & editing. Q.Y.: Conceptualization, Supervision, Writing—review & editing. D.H.: Resources,

Supervision, Writing—review & editing. All authors have read and agreed to the published version of the manuscript.

Funding: This research was funded by Shaanxi Province Natural Science Basic Research Program, grant number (2026JC-JCQN-115); Shaanxi Agricultural Science and Technology Innovation Project (NYKJ-2025-(XA)11).

Data Availability Statement: The data presented in this study are available on request from the corresponding author. The data are not publicly available due to privacy.

Acknowledgments: The authors acknowledge Azure Aviation Technology Ltd. for technical support in UAV-borne hyperspectral data acquisition. The authors further acknowledge China Chemical Geology and Mine Bureau for conducting the determination of soil organic carbon content.

Conflicts of Interest: The authors declare no conflicts of interest.

References

1. Xie, S.; Wang, X.; Zhu, X.; Li, Y. Prediction of Soil Organic Matter Content in Winter Wheat Jointing Stage Based on UAV Multispectral and Machine Learning. *Measurement* **2025**, *256*, 118508. [CrossRef]
2. Petersson, T.; Antoniella, G.; Perugini, L.; Chiriacò, M.V.; Chiti, T. Carbon Farming Practices for European Cropland: A Review on the Effect on Soil Organic Carbon. *Soil Tillage Res*. **2025**, *247*, 106353. [CrossRef]
3. He, L.; Lu, S.; Wang, C.; Mu, J.; Zhang, Y.; Wang, X. Changes in Soil Organic Carbon Fractions and Enzyme Activities in Response to Tillage Practices in the Loess Plateau of China. *Soil Tillage Res*. **2021**, *209*, 104940. [CrossRef]
4. Odebiri, O.; Mutanga, O.; Odindi, J. Deep learning-based national scale soil organic carbon mapping with Sentinel-3 data. *Geoderma* **2022**, *441*, 115695. [CrossRef]
5. Loiseau, T.; Chen, S.; Mulder, V.L.; Román Dobarco, M.; Richer-de-Forges, A.C.; Lehmann, S.; Bourennane, H.; Saby, N.P.A.; Martin, M.P.; Vaudour, E.; et al. Satellite Data Integration for Soil Clay Content Modelling at a National Scale. *Int. J. Appl. Earth Obs. Geoinf*. **2019**, *82*, 101905. [CrossRef]
6. Narimani, M.; Pourreza, A.; Moghimi, A.; Farajpoor, P. Sentinel-2 for Crop Yield Estimation: A Systematic Review. *Smart Agric. Technol*. **2026**, *14*, 102405. [CrossRef]
7. Li, S.; Li, X.; Ge, X. Prediction and Mapping of Soil Organic Carbon in the Bosten Lake Oasis Based on Sentinel-2 Data and Environmental Variables. *Int. Soil Water Conserv. Res*. **2025**, *13*, 436–446. [CrossRef]
8. Peng, Y.; Zhao, L.; Hu, Y.; Wang, G.; Wang, L.; Liu, Z. Prediction of Soil Nutrient Contents Using Visible and Near-Infrared Reflectance Spectroscopy. *ISPRS Int. J. Geo-Inf*. **2019**, *8*, 437. [CrossRef]
9. Zhen, Z.; Jianye, D.; Yang, Z.; Yinghui, Z.; Qingbin, W. Key Laboratory of Sustainable Forest Ecosystem Management. *Coll. For. Natl. Remote Sens. Bull*. **2025**, *29*, 2671–2685. [CrossRef]
10. El Bouanani, N.; Laamrani, A.; Ouzemou, J.-E.; Bouhnidira, A.; Ait Abdelali, H.; Bourriz, M.; Bourzeix, F.; Misbah, K.; Lazaar, A.; Chehbouni, A. Reconstructing Water Vapor Absorption Bands in PRISMA Hyperspectral Data for Improved Soil Total Nitrogen Estimation. *Smart Agric. Technol*. **2026**, *14*, 102184. [CrossRef]
11. Yan, Y.; Wang, J.; Miao, J.; Xu, Z. Small-sample soil organic carbon spectral estimation based on deep generative models and transfer learning. *Smart Agric. Technol*. **2026**, *15*, 102618. [CrossRef]
12. Meng, X.; Bao, Y.; Liu, J.; Liu, H.; Zhang, X.; Zhang, Y.; Wang, P.; Tang, H.; Kong, F. Regional Soil Organic Carbon Prediction Model Based on a Discrete Wavelet Analysis of Hyperspectral Satellite Data. *Int. J. Appl. Earth Obs. Geoinf*. **2020**, *89*, 102111. [CrossRef]
13. Dhiman, G.; Bhattacharya, J.; Roy, S. Soil Textures and Nutrients Estimation Using Remote Sensing Data in North India—Punjab Region. *Procedia Comput. Sci*. **2023**, *218*, 2041–2048. [CrossRef]
14. Liu, K.; Wang, Y.; Wang, X.; Sun, Z.; Song, Y.; Di, H.; Yan, Q.; Hua, D. Characteristic Bands Extraction Method and Prediction of Soil Nutrient Contents Based on an Analytic Hierarchy Process. *Measurement* **2023**, *220*, 113408. [CrossRef]
15. Mashori, A.S.; Li, F.; Aman, M.; Zhang, W.; Jia, S.; Ali, A.; Jabeen, N.; Hao, W.; Yan, Y. Remote Sensing through UAVs for Precision Agriculture: Applications, Technical Foundations, Current Barriers, and Future Opportunities. *Smart Agric. Technol*. **2026**, *14*, 102074. [CrossRef]
16. Yang, H.; Ma, L.; Wang, L.; Wang, R.; Chen, W.; Wang, L. Mapping Organic Carbon Content in Black Soil Using UAV Hyperspectral Remote Sensing and Deep Learning. *Earth Sci*. **2025**, *50*, 3144–3152. [CrossRef]
17. Zhu, Y.; Wang, D.; Zhang, H.; Shi, P. Soil organic carbon content retrieved by UAV-borne high resolution spectrometer. *Trans. Chin. Soc. Agric. Eng*. **2021**, *37*, 66–72. [CrossRef]

18. Liu, J.; Zhang, Y.; Wang, H.; Du, Y. Study on the Prediction of Soil Heavy Metal Elements Content Based on Visible Near-Infrared Spectroscopy. *Spectrochim. Acta A* **2018**, *199*, 43–49. [CrossRef]
19. Liu, K.; Wang, Y.; Peng, Z.; Xu, X.; Liu, J.; Song, Y.; Di, H.; Hua, D. Monitoring Soil Nutrients Using Machine Learning Based on UAV Hyperspectral Remote Sensing. *Int. J. Remote Sens.* **2024**, *45*, 4897–4921. [CrossRef]
20. Azizabadi, E.C.; Gomroki, M.; El-Shetehy, M.; Singh, K.D.; Mossa, A.-W.; Badreldin, N. VNIR-SWIR Hyperspectral Spectroscopy for Nitrogen Assessment in Potato Crops: Deep Learning and Regression Models across Field and Laboratory Conditions. *Smart Agric. Technol.* **2026**, *13*, 101801. [CrossRef]
21. Berhanu, K.T.; Ashilenje, D.S.; Ouzemou, J.-E.; El Battay, A.; Hajaj, S. Enhancing soil nutrient prediction accuracy using a robust UAV-based modeling framework in dryland environments. *Smart Agric. Technol.* **2026**, *14*, 102360. [CrossRef]
22. Zhang, J.; Ding, J.; Tan, J.; Wang, J.; Zhang, Z.; Wang, Z.; Ge, X. Monitoring Soil Salinization in Arid Cotton Fields Using Unmanned Aerial Vehicle Hyperspectral Imagery. *Int. J. Appl. Earth Obs. Geoinf.* **2025**, *140*, 104584. [CrossRef]
23. Gu, X.; Wang, Y.; Sun, Q.; Yang, G.; Zhang, C. Hyperspectral Inversion of Soil Organic Matter Content in Cultivated Land Based on Wavelet Transform. *Comput. Electron. Agric.* **2019**, *167*, 105053. [CrossRef]
24. Zhang, H.; Shen, Y.; Lv, H.; Wang, R. Hyperspectral Estimation of Soil Organic Matter Using Improved Spotted Hyena Optimizer and Iteratively Retained Informative Variables. *Microchem. J.* **2025**, *212*, 113410. [CrossRef]
25. Han, Y.; Zhang, X.; Zhang, Y.; Zhang, X.; Liu, H.; Ai, H.; Meng, X. Integrating Soil Stratification, Spectral Feature Parameters, and a Novel Deep Learning Model for Accurate SOM Prediction Using Vis-NIR Hyperspectral Data. *Soil Tillage Res.* **2026**, *263*, 107297. [CrossRef]
26. Guyon, I.; Weston, J.; Barnhill, S.; Vapnik, V. Gene Selection for Cancer Classification Using Support Vector Machines. *Mach. Learn.* **2002**, *46*, 389–422. [CrossRef]
27. Wang, S.; Guan, K.; Zhang, C.; Lee, D.; Margenot, A.J.; Ge, Y.; Peng, J.; Zhou, W.; Zhou, Q.; Huang, Y. Using Soil Library Hyperspectral Reflectance and Machine Learning to Predict Soil Organic Carbon: Assessing Potential of Airborne and Spaceborne Optical Soil Sensing. *Remote Sens. Environ.* **2022**, *271*, 112914. [CrossRef]
28. Tan, K.; Ma, W.; Chen, L.; Wang, H.; Du, Q.; Du, P.; Yan, B.; Liu, R.; Li, H. Estimating the Distribution Trend of Soil Heavy Metals in Mining Area from HyMap Airborne Hyperspectral Imagery Based on Ensemble Learning. *J. Hazard. Mater.* **2021**, *401*, 123288. [CrossRef]
29. Tang, A.; Yang, G.; Li, Z.; Pan, Y.; Liu, Y.; Long, H.; Chen, W.; Zhang, J.; Yang, Y.; Yang, X.; et al. Estimation of SOC Using VNIR and MIR Hyperspectral Data Based on Spectral-to-Image Transforming and Multi-Channel CNN. *Comput. Electron. Agric.* **2025**, *231*, 109986. [CrossRef]
30. Beisekenov, N.; Banakinaou, W.; Ajayi, A.D.; Hasegawa, H.; Tadao, A. Remote Sensing-Based Soil Organic Carbon Monitoring Using Advanced Machine Learning Techniques under Conservation Agriculture Systems. *Smart Agric. Technol.* **2025**, *11*, 101036. [CrossRef]
31. Durán-Rosal, A.M.; Ashley, T.; Pérez-Rodríguez, J.; Fernández-Navarro, F. Global and Diverse Ensemble Model for Regression. *Neurocomputing* **2025**, *647*, 130520. [CrossRef]
32. Huang, H.; Fang, Z.; Xu, Y.; Lu, G.; Feng, C.; Zeng, M.; Tian, J.; Ping, Y.; Han, Z.; Zhao, Z. Stacking and ridge regression-based spectral ensemble preprocessing method and its application in near-infrared spectral analysis. *Talanta* **2024**, *276*, 126242. [CrossRef]
33. Vavlas, N.-C.; Porre, R.; Meng, L.; Elhakeem, A.; van Egmond, F.; Kooistra, L.; De Deyn, G.B. Cover Crop Impacts on Soil Organic Matter Dynamics and Its Quantification Using UAV and Proximal Sensing. *Smart Agric. Technol.* **2024**, *9*, 100621. [CrossRef]
34. Canero, F.; Rodriguez-Galiano, V.; Aragones, D. Machine Learning and Feature Selection for soil spectroscopy. An evaluation of Random Forest wrappers to predict soil organic matter, clay, and carbonates. *Heliyon* **2024**, *10*, 30228. [CrossRef]
35. Chang, N.; Jing, X.; Zeng, W.; Zhang, Y.; Li, Z.; Chen, D.; Jiang, D.; Zhong, X.; Dong, G.; Liu, Q. Soil Organic Carbon Prediction Based on Different Combinations of Hyperspectral Feature Selection and Regression Algorithms. *Agronomy* **2023**, *13*, 1806. [CrossRef]
36. Vlachakis, D.; Kasimati, A.; Zafeiriou, I.; Espejo-Garcia, B.; Fountas, S. Estimation of soil properties using Hyperspectral imaging and Machine learning. *Smart Agric. Technol.* **2025**, *10*, 100790. [CrossRef]
37. Alsaleh, A.R.S.; Alcibahy, M.; Gafoor, F.A.; Al Hashemi, H.; Athamneh, B.; Al Hammadi, A.A.; Seneviratne, L.; Al Shehhi, M.R. Estimation of Soil Organic Carbon in Arid Agricultural Fields Based on Hyperspectral Satellite Images. *Geoderma* **2025**, *453*, 117151. [CrossRef]
38. Yang, J.; Li, X.; Ma, X. Improving the Accuracy of Soil Organic Carbon Estimation: CWT-Random Frog-XGBoost as a Prerequisite Technique for In Situ Hyperspectral Analysis. *Remote Sens.* **2023**, *15*, 5294. [CrossRef]
39. Han, Y.; Wang, B.; Yang, J.; Yin, F.; He, L. Research on Hyperspectral Inversion of Soil Organic Carbon in Agricultural Fields of the Southern Shaanxi Mountain Area. *Remote Sens.* **2025**, *17*, 600. [CrossRef]

40. Piccini, C.; Metzger, K.; Debaene, G.; Stenberg, B.; Götzinger, S.; Borůvka, L.; Sandén, T.; Bragazza, L.; Liebisch, F. In-field soil spectroscopy in Vis-NIR range for fast and reliable soil analysis: A review. *Eur. J. Soil Sci*. **2024**, *75*, e13481. [CrossRef]
41. McGuirk, S.L.; Cairns, I.H. Relationships between Soil Moisture and Visible-NIR Soil Reflectance: A Review Presenting New Analyses and Data to Fill the Gaps. *Geotechnics* **2024**, *4*, 78–108. [CrossRef]

Disclaimer/Publisher's Note: The statements, opinions and data contained in all publications are solely those of the individual author(s) and contributor(s) and not of MDPI and/or the editor(s). MDPI and/or the editor(s) disclaim responsibility for any injury to people or property resulting from any ideas, methods, instructions or products referred to in the content.